5-2022

Nanostructured Materials for Biomedical Applications

Silverio Lopez
The University of Texas Rio Grande Valley

NANOSTRUCTURED MATERIALS FOR BIOMEDICAL APPLICATIONS

A Thesis

by

SILVERIO LOPEZ

Submitted in Partial Fulfillment of the
Requirements for the Degree of
MASTER OF SCIENCE

Major Subject: Biochemistry and Molecular Biology

The University of Texas Rio Grande Valley

May 2022

NANOSTRUCTURED MATERIALS FOR BIOMEDICAL APPLICATIONS

A Thesis

by

SILVERIO LOPEZ

COMMITTEE MEMBERS

Dr. Karen Martirosyan

Chair of Committee

Dr. Ahmed Touhami

Committee Member

Dr. Megan Keniry

Committee Member

May 2022

ABSTRACT

Lopez, Silverio, Nanostructured Materials for Biomedical Applications. Master of Science (MS), May, 2022, 67 pages, 6 tables, 21 figures, references, 113 titles.

Nanotechnology has been used in an increasing number of applications in biochemistry and molecular biology. Compared to bulk materials, nanoscale materials offer a variety of advantages in applications due to an increased surface-to-volume ratio of the reactants. The unique properties of nanostructured materials and their properties such as stability, reactivity, magnetic response, pressure discharge performance and biocompatibility depend on particle size and shape. This work focuses on a nanoenergetic material composed of Aluminum (Al), Copper II oxide (CuO), and Iodine (I) pentoxide (I2O5), and the biomedical application of nanoscale dextran-coated magnetite (Fe3O4), which was produced using microfluidics to tune particle size. E. coli was shown to be sensitive to the reaction of the NM and the gaseous species produced during the reaction. The ionized Cu and I likely interacted with the bacterial proteins, lipids, and DNA, which led to cell death. In addition, the E. coli was sensitive to heating caused by magnetic induced hyperthermia in the presence of dextran-coated superparamagnetic iron oxide nanoparticles (SPIONs). Further, SPIONs were used to provide controlled drug release of minocycline housed in a poly(lactic-co-glycolic acid) (PLGA) scaffold in an alternating magnetic field. SPIONs in an alternating magnetic field exhibited hyperthermia, due to nanoscale particles (10nm) becoming single magnetic domains, which have the potential to both treat tumor cells, and aid diagnostics and concomitant treatment modalities. Further modification of the SPIONs with dextran as a

surfactant both served to control particle size and increase the intimate interaction with E. coli, allowing for the particles to exhibit a biocidal effect via magnetic induced hyperthermia.

DEDICATION

This thesis is dedicated to my loved ones, without whom this would have been much more difficult. I cannot thank them enough for the support they have provided me. To each and every person who has helped me, thank you. I , in no way, would have been capable of achieving what I have, without your help.

ACKNOWLEDGMENTS

I want to express my gratitude to all those who have me along the way, I would not be where I am today without them. I want to thank Dr. Martirosyan for pushing me to achieve things I did not think I would. I also want to thank Carlos Trevino De Leo, Ivan Davila, Mkhitar Hobosyan, and Zuzanna Lawera for serving not only as mentors, but as friends from whom I learned much from. I also want to thank my committee members, Dr. Ahmed Touhami, and Dr. Megan Keniry who have had a major role in my academic growth while I pursued my Masters degree. This dissertation contains parts from a paper I have aided in publishing with research groups, and I want to thank my co-authors who helped guide me throughout the ordeal, especially Marco Arriaga, and Sue Anne Chew who pushed me to pursue research.

TABLE OF CONTENTS

Page

ABSTRACT……..iii

DEDICATION…..……....v

ACKNOWLEDGMENTS……...……v

TABLE OF CONTENTS……..vii

LIST OF TABLES……..ix

LIST OF FIGURES…….……....x

CHAPTER I. INTRODUCTION…….....1

1.1 Statement of the Problem.……...……...1

1.2 Statement of the Purpose……..…….……..…4

CHAPTER II. LITERATURE REVIEW …….……...6

2.1 Pathogens: Structure and Survival……..…….. 6

2.2 Antimicrobial Nanomaterials……..……...…….9

2.3 Metals in Biochemistry……...…..12

2.4 Magnetic Nanoparticles……...….22

2.5 Heating Mechanism of Magnetic Nanoparticles……...…23

2.6 Specific Power Absorption and Effect of Heat on Cells…….....25

2.7 Modification of SPIONs for Improving Biomedical Applications……...…30

CHAPTER III. MATERIALS AND METHODS…….....37

3.1 Preparation of (10Al+3I2O5)-n wt% (2Al-3CuO) Nanothermite Mixtures…….....37

3.2 Thermodynamic Analysis for the Al-CuO-I2O5 systems…….....38

3.3 Pressure Discharge Testing of the Nanoenergetic mixtures……..…….....…39

3.4 X-Ray Diffraction……...…….....40

3.5 Scanning Electron Microscopy and Energy Dispersive X-Ray Spectroscopy…..…..41

3.6 Escherichia coli and Agar Plate Preparation……...….41

Page

3.7 Assessing Biocidal Properties of the Nanoenergetic Mixture…….....42

3.8 Microfluidic Synthesis of Dextran coated Superparamagnetic Nanoparticles……43

CHAPTER IV. FINDINGS AND DISCUSSIONS…….……...45

4.1 Thermodynamic Analysis of the Al-CuO-I2O5 systems…...…….....…….45

4.2 Pressure Discharge values of the Nanoenergetic mixtures……...…….....…...47

4.3 Crystallinity of Al-CuO-I2O5 Reaction Product……...…….....48

4.4 Surface Morphology and Elemental Composition of the Nanoenergetic Systems..…49

4.5 Biocidal Test of 50%Al-CuO – 50% Al-I2O5…….…....52

4.6 Crystallinity of SPIONs.……...…….....54

CHAPTER V. CONCLUSION…….……..56

REFERENCES…….....…..58

BIOGRAPHICAL SKETCH……..….67

LIST OF TABLES

Page

Table 1: Contact Killing times of Pathogens on Copper Surfaces…..……17

Table 2: Independent Systems contributing to the
(10Al +2I2O5) -n wt% (2Al+3CuO) Nanoenergetic systems……45

Table 3: Weight and Atomic Percent of the Al-25%CuO-75%I2O5 NM system……..50

Table 4: Weight and Atomic Percent of the Al-50%CuO-50%I2O5 NM system……51

Table 5: Weight and Atomic Percent of the Al-75%CuO-25%I2O5 NM system……..52

Table 6: Images of the agar plates exposed to the nanoenergetic reaction within
the testing chamber and their respective % inhibition of E. coli colony formation……..53

LIST OF FIGURES

Page

Figure 1: (A) Gram-positive bacteria and (B) gram-negative bacterial cell wall..……..……...7

Figure 2: (A) Enveloped Virus components and (B) Naked Virus.…….…....9

Figure 3: Fenton Type Reaction…….……...14

Figure 4: Effect of Metal Oxide nanoparticles on cells…….……14

Figure 5: Neel and Brownian Relaxation…….…..25

Figure 6: SPION modified for various biomedical applications…….……..……31

Figure 7: Cell viability for U87 cells treated with different concentrations of Fe3O4 NPs**……..**32

Figure 8: Cumulative drug release (%) of PLGA scaffolds
fabricated with minocycline placed at 37 versus 42◦C……..…33

Figure 9: Change in temperature over 60 min for PLGA
scaffolds made with minocycline and different wt. % of Fe3O4 nanoparticles……34

Figure 10: Cell viability of U87-MG glioblastoma cells exposed to elevated temperatures...….35

Figure 11: Pressure Discharge DAQ apparatus……..…...…..……...……...….40

Figure 12: Illustration of the testing chamber and respective heights and orientation of each agar
plate……..…43

Figure 13: Graphic depicting set up of Microfluidic Assisted Synthesis of SPIONs……...…44

Figure 14: Adiabatic temperature of combustion and product composition
dependence on the weight percentage of Al-CuO formulation
in the system ($10Al+3I_2O_5$) -n wt% (2Al+3CuO)…….46

Figure 15: Pressure Discharge values of the varying wt.%
ratios of the Al-CuO-I2O5 nanoenergetic systems……...47

Figure 16: XRD of (A) Purchased CuI, (B) 50%Al-CuO–50%Al-I2O5,
(C) 75%Al-CuO–25% Al-I2O5, and (D) 25%Al-CuO–75%Al-I2O5..……49

Figure 17: SEM images of the 25%Al-CuO–75%Al-I2O5 nano-formulation……...……..50

Figure 18: SEM images of the 50%Al-CuO–50%Al-I2O5 nano-formulation……..…51
Figure 19: SEM images of the 75%Al-CuO–25%Al-I2O5 nano-formulation…….....52
Figure 20: Frames from the slowmotion video of the NM reaction……..53
Figure 21: XRD of Dextran-Coated Iron Oxide Nanoparticles……55

CHAPTER I

INTRODUCTION

1.1 Statement of the Problem

The ability pathogens have to persist in the environment for great lengths of time is major problem in healthcare, leading to increasing overall cost of healthcare and additional infections that could otherwise be avoided and/or prevented. As an example, hospital acquired infections (HAIs) are responsible for a great increase in the total cost associated with treatment (Osme et al., 2021). One study observed the financial impact of healthcare-associated infections just within the intensive care units (ICUs) of 50 hospitals, looking specifically at patients who did or did not acquire HAIs. It was found that patient's who suffered from a HAI required treatment for two weeks longer on average and wound up paying over US $13,000 extra compared to patient's who did not suffer from HAIs (Osme et al., 2021). They took the annual direct cost of over 26,000 patients across the 50 hospital's ICU facilities, US $112,924,421, and extrapolated to determine that in the event of just 29% HAIs, there would be an increase of US $147 million. For a situation with a 61% HAIs, there would be an increase of US $147 million to the annual direct cost (Osme et al., 2021). This study performed in 2021, looking at just 50 hospitals shows the direct financial burden that HAIs have in a healthcare setting. During the 2019 Covid pandemic, hospitals were flooded with patients, including those who required non-Covid related care. Specifically, bacteria are responsible for an estimated 90% of cases and 10% are attributed to fungi (Mitchell, 2021).

Pathogens, within a health-care setting, are primarily transferred from infected patients and staff; however, high-touch surfaces also contribute to disease transmittance (Kramer, 2014). The ability of pathogens to contribute to HAIs is largely due to their capability to persist in their environment for great lengths of time, a factor that varies greatly depending on the pathogen. For example, Staphylococcus aureus (S. aureus) can persist for anywhere from 7 days to 1 year, and Escherichia coli (E. coli) can persist from between several hours to 16 months depending on the environment (Mitchell, 2021). The environment highly contributes to the length of time a pathogen can persist, namely the humidity, temperature, and whether an organism can produce a biofilm (Mitchell, 2021), (Murray et al., 2015). Biofilms, produced by bacteria, are a polysaccharide coating that encapsulates and protects the bacteria when sufficient numbers are present, and the environment supports biofilm production. Pathogens are constantly challenged in changing environments due to stressors such as temperature change, heavy metal exposure, osmotic stress, and nutrient depletion; thus, they have evolved defense systems to regulate gene expression in accordance with their environment (Murray et al., 2015; Ron, 2006). Also of note, is that gram positive bacteria tend to fare better in drier conditions than gram negative bacteria, likely due to their differing cell wall structure (Mitchell, 2021); i.e., gram-positive bacteria have a thick peptidoglycan cell wall, while gram-negative bacteria have an outer membrane comprised of lipopolysaccharides as well as porins in addition to a periplasmic space housing lipoproteins. Aside from just bacteria, other pathogens such as viruses and fungi attribute to HAIs as well. Virus persistence in the environment is highly dependent on whether a virus is enveloped or non-enveloped, as the former requires aerosolized micro-droplets that can dry at varying rates according to surface topography and humidity (CDC, 2019). In general, stainless steel and polymer-based touched surfaces are typically utilized in healthcare setting because they appear clean when wiped with typical cleaning

solutions; however, surfaces as these rely on chemicals, and more importantly, the staff for maintaining sanitation (Lei et al., 2017). Another major problem that is of growing concern is that of cancer. The NIH (NIH, 2021) estimated in 2020, 1,806,590 cases of cancer of cancer were diagnosed. According to estimates based on recent data, approximately 39.5% of men and women will face a cancer diagnosis in their lifetime. Cancer alone was responsible for over $150 billion of US spending on health-care. Further, cancer is currently the leading cause death the world over. Extrapolating given current data, the NIH predicts that by 2040 the number of new cases of cancer each year will reach 29.5 million (NIH, 2021). Being a disease with a genetic origin, cancer is notoriously difficult to treat despite an abundance of advancements in characterization and treatment. Currently, many of the treatments employed in treating cancer remain toxic not only to the cancer cells, but to the healthy host cells (Chakraborty and Rahman, 2012), causing systemic side effects that decrease prognosis and lessen morale of the patient. The toxic effects of chemotherapeutics coupled with the drugs non-specificity result systemic toxic effects in the patient. Adding to the complexity of the problem, is the tendency of cancer to metastasize, that is, after a length of time (which varies according to the aggressiveness of the cancer), the cancer will spread to different areas of the body (Chakraborty and Rahman, 2012), a phenomenon known as metastasis.. Metastasis occurs as the cells grow and divide uncontrollably, invading local tissues as well as blood vessels and the lymphatic system, making drug-targeting and treatment increasingly difficult since the disease gets increasingly complex to pinpoint for treatment. Fortunately, through the efforts of many scientists, new materials are being developed and researched with promising outlooks that can serve to benefit many as novel treatment methods are implemented. .

1.2 Statement of the Purpose

Nanomedicine offers exciting new applications for treating cancer. Using nanostructured materials that are biocompatible and easily absorbed or excreted allows for researchers to more increase site-specificity of current treatments and prolong the plasma concentration (Pucci et al., 2019). Nanomaterials are not just suited for treatment, depending on the material they can be used for diagnosis as well, or for simultaneous treatment and diagnosis, a phenomenon termed "theranostics" (Matea et al., 2017). In addition, the use of nanomaterials to increase site-specificity directly increases the efficacy of any chemotherapeutics, meaning that less drug is required for treatment; thereby, effectively decreasing any unwanted systemic side-effects. It follows then, that alternative sanitization, disinfection, and treatment methods based on nanomaterials are warranted to slow the progression of drug-resistant pathogens and cancer rates, as well as contribute overall to the quality of healthcare by offering tailored treatments.

In this work, a novel ternary nanoenergetic material (NM) comprised of Aluminum (Al), Copper (II) Oxide (CuO), and Iodine Pentoxide (I2O5) is synthesized and its biocidal efficacy is tested to determine its potential application as a supplementary sanitation method in healthcare and communal settings. The NMs used in this study are comprised of oxidizers (metal or non-metal oxides) and a fuel (metal nanoparticles) (Hobosyan and Martirosyan, 2020; Puszynski et al., 2007; Dlott, 2006; Hobosyan and Martirosyan, 2017). Using nano-scale constituents as opposed to micron-scale is beneficial as the reactivity of NMs increases when its constituents are on the nanoscale. As particle's surface area to volume ratio increases which increases the intimate contact between the oxidizers and metal fuel (Sun, 2006). The novel use of an NM to spatially disinfect areas offers the potential to reduce the financial and medical burdens in the healthcare field by reducing the presence of pathogens. Previously Al-I2O5 systems have been shown to reduce the

number of colonies grown on agar plates following exposure to the reactions (Clark and Pantoya, 2010; Martirosyan et al., 2011), suggesting that the generation of gaseous iodine and copper, in conjunction with the pressure produced, can aid in spatial disinfection. In addition, Superparamagnetic Iron Oxide particles (SPIONs) produced via microfluidic assisted co-precipitation were also investigated for use in a novel cancer treatment method. SPIONs can be functionalized with various surface ligands to achieve concomitant imaging and treatment of bacteria and cancer. SPIONs, at the critical size of ˜50nm exhibit superparamagnetic properties (Ohannesian, 2019). Within an alternating magnetic field, the SPIONs line up with the field as it changes, causing a phenomenon known as magnetic induced hyperthermia which can be used to heat the surrounding medium, be it tissue or fluid. For this reason, SPIONs have much potential for biomedical applications. The microfluidic assisted synthesis of SPIONs along with their subsequent use for tuning minocycline release is also discussed.

CHAPTER II

LITERATURE REVIEW

2.1 Pathogens: Structure and Survival

Bacteria can persist for various lengths of time according to environmental factors as well as whether the bacterium in question is gram negative or gram positive (Mitchell, 2021; Murray et al., 2015; Ron 2006). Gram-positive bacteria have a thick outer peptidoglycan layer, comprised or lipotechoic and techoic acids, while gram-negative bacteria have a peptidoglycan layer that houses proteins, phospholipids, and lipopolysaccharides (Murray et al., 2015). Peptidoglycan is essential for replication, structure, and bacterial survival in various environments, which may be why gram-positive bacteria display increased survivability in drier conditions (Mitchell, 2021). The survivability of bacterium is not strictly dependent on persistence, but antibiotic-resistance as well since antibiotics are generally the primary treatment modality (Jung et al., 2019), particularly in health-care facilities where patients are seeking care. 'Resistance' refers to a bacterium's ability to resist the effects of antibiotics by one or more mechanism, such as by enzymes to degrade the drug, via membrane pumps which remove the drug from the cytoplasm, or by altering the targeted protein's conformation (Blair et al., 2015). 'Persistent' bacteria, however, tend to be sensitive to antibiotics or disinfectants, though they present with a 'tolerant' phenotype that allows them to persist in their environment (Jung et al., 2019).

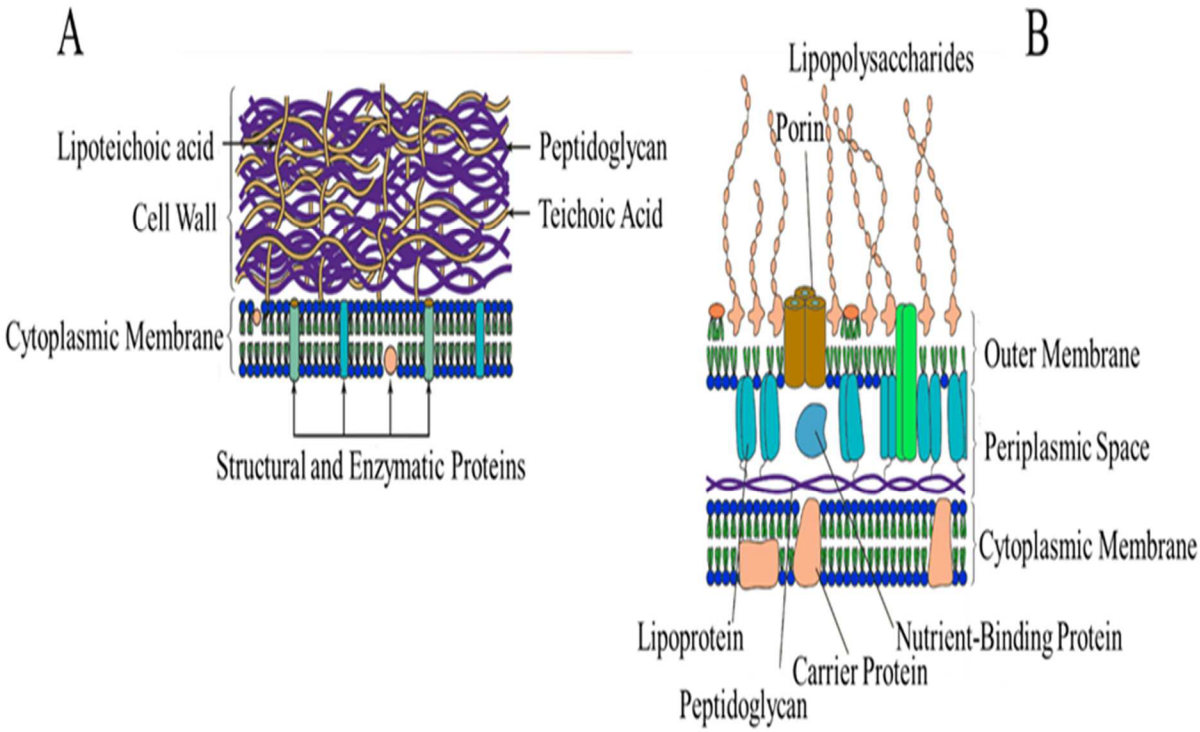

Figure 1: (A) Gram-positive bacteria and (B) gram-negative bacterial cell wall

In example, persistent bacteria may produce biofilms more rapidly in response to environmental, or other, stressors. Bacterial persistence is thought to be a stress-response that is induced due to antibiotic treatment. It is a phenomenon that has been inherited by both gram-positive and gram-negative bacteria, as both form 'persister' subpopulations when treated with antibiotics (Bergh et al., 2017). The main mechanism through which persisters increase their survivability is through dormancy, which they enter in response to changes in their environment, such as toxin presence, temperature fluctuations, and pH changes (Jung et al., 2019). Bacteria are faced with a trade-off in the case of antibiotic resistance, in that their survivability is diminished when the antibiotic pressure is relieved; however, with persistence, there is no cost to fitness (Massey et al., 2001).

Balaban's group were able to isolate an E. coli subgroup of resistant cells that exhibited a decreased growth rate even before treatment with ampicillin (Balaban et al., 2004), which led his team to believe that the persistent bacteria were in a protected part of their cell cycle. While dormant, the bacterial cells cease translation, transcription, and ATP production (Kim et al., 2018). Thus, aside from the ever-growing problem of antibiotic resistance, bacterial persistence contributes to the threat of healthcare-associated infections.

Similarly, viruses and fungi can persist in health-care facilities for varying lengths of time, lengths that are highly dependent on environmental factors. Namely, relative humidity, temperature, and the material character of the surface they reside on (Kramer, 2014). Viruses vary greatly, containing either DNA or RNA, though they can generally be classified as having (enveloped) or not having (naked) a membrane surrounding their protein coat (capsid) (Murray et al., 2015) (Figure 2). Naked viruses rely on their capsid for protection in their environment, and as a result can endure a range of conditions, such as sewage, dry conditions, extreme changes in pH, and detergents. The membranes of enveloped viruses are composed of lipids, glycoproteins, and proteins, and as a result they must remain wet. Thus, enveloped viruses are susceptible to solvents, detergents, drying, and fluctuations of pH, which is why they are generally transmitted through fluids and tissue (Murray et al., 2015). Many of the respiratory viruses, such as Corona-, Influenza virus, and rhinovirus are enveloped and as such, persist for days on surfaces before they become inactivated (Casanova et al., 2010), while the astrovirus (a naked virus) has been shown to survive for up to 90 days (Abad et al., 2001). Similarly, fungi, though sensitive to changes in the environment, can survive on surfaces for great lengths of time as well. For instance, *Candida albicans*, responsible for yeast infections, has been shown to survive in the environment for up to 120 days (Theraud et al., 2003).

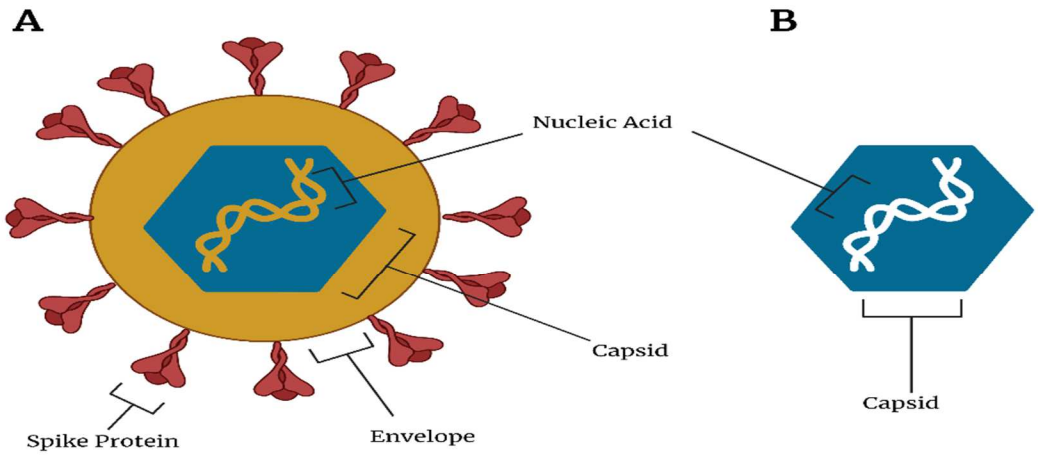

Figure 2: (A) Enveloped Virus components and (B) Naked Virus

Persistence and resistance are major problems, because the world over due to the ever-growing problem of antibiotic resistance. In fact, the World Health Organization (WHO) listed antibiotic resistance as one of the top three most dire public health threats of the 21st century (WHO, 2014). To mitigate the development of more and more resistant strains of bacteria, nanoparticles/-media can be looked to. Nanoparticles, ie, particles with dimension below 100nm have surfaced as key components in modern medicine, with various clinical applications such as contrast for diagnostic imaging, drug carriers, and self-disinfecting surfaces (Murthy, 2007).

2.2 Antimicrobial Nanomaterials

Due to changes in properties of materials at the nanoscale, including higher surface-to-volume ratio, increased reactivity, unique optical and electronic properties, superparamagnetism, nanomaterials can be employed for a variety of applications. Nanomaterials are defined as

particles, organic/inorganic or hybrids, with sizes less than 500 nm (though the definition is ever evolving). At the nanoscale, materials can have a plethora of morphologies and structures, ranging from fibrous networks to rods to solid/hollow spheres to pyramids (Makabenta et al., 2021). At sizes of less than 500 nm, nanomaterials can intimately interact with pathogen membranes, intracellular structures, and a variety of biomolecules. Further, nanomaterials can be subclassified based on their composition, consisting of carbon-based NPs, nanocomposites, metal-based NPs, liposomes, and a variety of hybrids (Makabenta et al., 2021). Metal-based NPs can consist of pure metals (Ag, Cu, Au), or compounds such as their corresponding oxides of hydroxides. With metal-based nanoparticles their primary uses are that of their antimicrobial nature in which they result in destruction of cellular membranes or intracellular components by generating reactive oxygen species and displacing necessary functional groups on key enzymes and proteins by leeching reactive metal ions (Valko et al., 2005). Continuing, the carbon-based NPs, as the name suggests, are comprised of nanomaterials including carbon as a primary constituent. For example, carbon quantum dots, 2- and 3-d nanomaterials such as nanotubes and fullerene are such carbon-based nanomaterials (Makabenta et al., 2021). Carbon-based NPs offer a variety of applications, such as drug-shuttling to evade the bodies immune system and increase drug-delivery, and there has even been a study detailing the use of multi-walled carbon nanotubes to prevent formation of biofilms from various bacteria (Malek et al., 2016). Further, the polymeric NPs can consist of either synthetic or natural materials and can be used for mimicking the action of antimicrobial peptides, or as shuttles to improve drug-delivery by improving colloidal stability, solubility, and the pharmacokinetic efficacy of drugs (Landis et al., 2017). In one study, the researchers demonstrated that a crosslinked polymeric nanomaterial (250 nm) was able to penetrate and destroy various multidrug-resistant biofilms (Landis et al., 2017).

Carrying on, nanocomposites or hybrids, are nanomaterials consisting of two or more types of nanomaterials such as metal-based and polymeric NPs. By incorporating more than one type of NP into a nanocomposite, nanomaterials can be made to provide synergistic activity when treating a disease or pathogen (Makabenta et al., 2021). For example, a group of researchers developed a nontoxic nanocomposite comprised of Silver (Ag) and polymerized 2-(dimethylamino)ethyl methacrylate (DMAEMA) for use as an antimicrobial agent by inducing membrane disruption, penetrating cells, and inhibiting intracellular components. In addition, the researchers noted that the nanocomposite aided in healing of the P. aeruginosa and S. aureus induced infections they studied in model animals (Mei et al., 2014). Carrying on, nanocomposites or hybrids, are nanomaterials consisting of two or more types of nanomaterials such as metal-based and polymeric NPs. By incorporating more than one type of NP into a nanocomposite, nanomaterials can be made to provide synergistic activity when treating a disease or pathogen (Makabenta et al., 2021). For example, a group of researchers developed a nontoxic nanocomposite comprised of Ag and polymerized 2-(dimethylamino)ethyl methacrylate (DMAEMA) for use as an antimicrobial agent by inducing membrane disruption, penetrating cells, and inhibiting intracellular components. In addition, the researchers noted that the nanocomposite aided in healing of the P. aeruginosa and S. aureus induced infections they studied in model animals (Mei et al., 2014). Similarly, liposomes are nanomaterials composed of one or more phospholipid bilayers, similar to micelles, that are highly biocompatible and useful for drug-delivery (Makabenta et al., 2021). As they are membrane-based nanomaterials, liposomes can be used to envelop hydrophilic drugs that would other have difficulty passing cellular membranes. Liposomes can increase the efficacy of antibiotics by protecting them from degradation, inactivation, and improving targeting, as the liposome can directly fuse to bacterial cells (Forier et al., 2014). In addition, aside from just

enveloping hydrophilic drugs in their interior, hydrophobic drugs can be incorporated into their phospholipid membrane (Forier et al., 2014). Making use of various nanomaterials and their properties, "smart" nanomaterials can be developed. That is, nanomaterials that respond to their environmental stimuli such as changes in pH, temperature, light and the presence of antigens (Beta and Mondal, 2018). To design smart nanomaterials, it is necessary to keep in mind the factors important for maximizing therapeutic efficacy, such as drug-loading capability, permeability, circulation time, and site-specificity. Thus, smart nanomaterials must respond to a specific stimuli to ensure that the therapeutic activity is only present at the proper time. For example, one might wish for a nanomaterial to respond only when a certain temperature is reached at the target site, a magnetic field is applied, a certain wavelength of light is used for excitation, a mechanical force is exerted, or a certain pH is present (Bera and Mondal, 2018). As an example, researcher were able to produce poly(asparamide)-derived micelles using cationic copolymers as well as azithromycin-coupled and pH-sensing copolymers. The researchers then showed that the micelles responded to the acidic environment of a P. aeruginosa biofilm, causing the micelle to shrink in size from 107 nm to 54 nm, and inducing a change in surface charge from -11.7 mV to 26.4 mV, allowing the micelle to penetrate the biofilm and release the azithromycin via lipase triggered release (Chen et al., 2018). Overall, nanomaterials have a variety of applications, which can be further expanded through combining various classes of nanomaterials to confer various treatment modalities and drug-delivery capabilities synergistically.

2.3 Metals in Biochemistry

Though the mechanism was unknown to the ancients, metals such as Cu and Ag have long been used throughout history for their biocidal properties. For example Cu and Ag had been used

throughout history for various applications ranging from preserving water purity to preventing the growth of barnacles on ship's hulls, and as cooking utensils to prevent disease (Weber and Rutala, 2013; Grass et al., 2011; Lemire et al., 2013; Tamayo et al., 2016). Many organisms make use of metals for necessary biochemical reactions, neurotransmission, and maintaining a cationic environment and osmotic balance (Harrison and Hoare, 1980). More specifically, metals can be grouped into either the 'Main Group Metals' or the 'Transition Metals,' with main group metals, consisting of lithium (Li), Sodium (Na), Potassium (K), Magnesium (Mg), Calcium (Ca), as well as others that serve to primarily aid in electric excitability and assist in biochemical reactions as cofactors (Nogrady and Weaver, 2005). For example, Na and K are necessary for maintaining the excitability of the cardiac, neural and muscle cells. In addition, transition metals consist of Iron (Fe), Manganese (Mn), Cobalt (Co), Nickel (Ni), Copper (Cu), Zinc (Zn), and many others which serve both structural and functional roles in biochemistry (Nogrady and Weaver, 2005). For instance, Fe is essential for cellular respiration as it is the central atom in various Cytochrome molecules, and Cu is found in several enzymes such as, cytochrome c oxidase, cytosolic superoxide dismutase, catalase, peroxidases, and dopamine-beta-hydroxylase (Nogrady and Weaver, 2005; Barceloux and Barceloux, 1999). Specifically, Cu is the third most present trace element in the body and is necessary because it acts as a donor/acceptor of electrons, shifting between the Cu (I) and Cu (II) redox states (Karlin, 1993) aiding as a co-factor for the enzymes mentioned. It is, however, also the ability of Cu to alternate between redox states that also allows it to act detrimentally to cells in high concentrations, forming superoxide and hydroxide radicals through Fenton reactions (Valko et al., 2005; Festa and Thiele, 2011). Hydroxyl radicals that are generated in the intracellular space are free to interact with nucleic acids, proteins, lipids, and

enzymes, interfering with necessary biochemical reactions that maintain homeostasis (Festa and Thiele, 2011; Inesi, 2017).

$$Cu^{+} + H_2O_2 \rightarrow Cu^{2+} + OH^{-} + OH^{\cdot}$$

Figure 3: Fenton Type Reaction

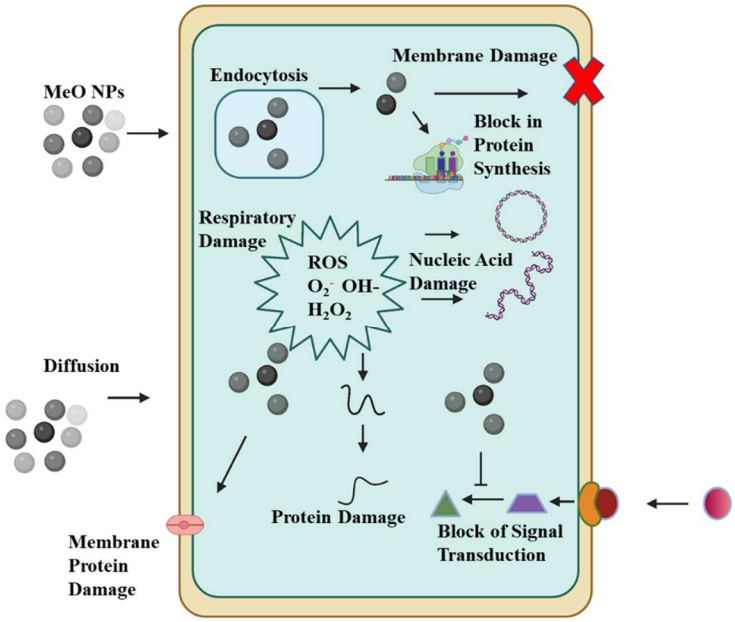

Figure 4: Effect of Metal Oxide nanoparticles on cells

In addition, free Cu ions can take other metal's places from their respective metalloprotein ligands, causing improper protein folding and activity (Festa and Thiele, 2011). Similarly, free Cu ions readily bond to thioether and thiol groups, commonly found in amino acids methionine and cysteine, along with oxygen or imidazole-bound nitrogen groups, of the aspartic and glutamic acid,

or histidine amino acids (Festa and Thiele, 2011). Thus, Cu has the ability to participate in a large array of interactions with various proteins and residues, lending to a variety of biocidal applications. That said, the implementation of Cu for antimicrobial surfaces or biocidal materials requires consideration of Cu's cytotoxic effects. Continuing on to Ag, though not a trace element in the human body, it does become present in the body through inhalation or ingestion (Marx and Barillo, 2014) and can be found in a large variety of industries. Ag in an ionized state has the ability to interact with a variety of moieties such as sulfhydryl, amino-, phosphate-, imidazole-, and carboxyl- groups to inactivate or denature proteins, and destroy cell walls of single cell bacteria (Wadhera and Fung, 2005; Fung and Bowen, 1996) which serve to hinder the survival and propagation of bacterial cells. For this reason, metal nanoparticles such as Cu and Ag have been widely employed for their antimicrobial properties; properties which, at the nanoscale, offer even further functionality.Formerly, the use of metals had largely diminished from what it once was due to the discovery and implementation of antibiotics, but metals are once again seeing use as antibiotic resistance becomes prevalent (WHO, 2014; Weber and Rutala, 2013; Grass et al., 2011; Lemire et al., 2013; (Tamayo et al., 2016; Silvestry-Rodriguez et al., 2007). Metal oxides, both in bulk and nanostate have been recognized for their antimicrobial capabilities and though the exact mechanism has not been determined, it is largely accepted that it is due to the aforementioned ability they have to induce reactive oxygen species (ROS) which hinders many cellular processes (Figure 3) (Valko et al., 2005; Festa and Thiele, 2011; Inesi, 2017; Marx and Barillo, 2014; Wadhera and Fung, 2005; Fung and Bowen, 1996). Cu has been studied extensively for its ability to kill microbes upon contact, in a time span ranging from minutes to hours depending on the copper content of the alloys used, incubation temperature, and inoculation technique used (Weber and Rutala, 2013; Grass et al., 2011). Though Cu clearly exhibits biocidal capabilities, it should

be noted that a comparison of the studies is not exact since the effects were not carried out using the same parameters; however, the findings from each study point to higher temperatures, relative-humidity, and Cu content of the alloys serving to increase the biocidal efficacy (Grass et al., 2011). More specifically, 1x1 cm coupons of Cu and various Cu alloys were sterilized and tested against various sensitive and antibiotic-resistant bacteria and pathogens. After culturing the bacteria until a high colony forming unit (CFU) per milliliter count was achieved, the researchers inoculated the various coupons with the different bacterial isolates and incubated them for varying time periods at room temperature to mimic exposure of high-touch surfaces in a health-care facility. Following incubation, the coupons were placed in a bottle of PBS with glass beads and centrifuged, before being serially diluted to inoculate agar plates. The colony growth was then examined to determine the effects of the Cu and various Cu alloys on bacterial growth (Mehtar et al., 2008). The killing curves were taken by analyzing and plotting the colony growth of each pathogen recovered after exposure to the coupons from varying times. *Candida albicans, Klebsiella pneumoniae, Pseudomonas aeruginosa, Acinetobacter baumannii*, and Methicillin-Resistant *Staphylococcus aureus* (MRSA) were evaluated, and in each instance, it was found that Cu and Cu alloys were most effective at reducing CFU count in less time (Mehtar et al., 2008). *C. albicans* and *K. pneumoniae* experienced a total reduction in CFU count in 60 minutes, while P. aueruginosa, A. baumannii, and MRSA took 180 minutes to achieve a 100-fold reduction (Mehtar et al., 2008). The researchers demonstrated that pure Cu or the Cu alloys with higher Cu % by wt. should be used to achieve more rapid and efficacious destruction of pathogens, with the minimum concentration of Cu being 55% for bacteria (Mehtar et al., 2008). Similarly, Noyce and colleagues tested the effects of Cu, Brass (80 % Cu and 20% Zinc (Zn)), Zn, and Stainless steel (SS) using the same methods as Elguindi's team (Mehtar et al., 2008; Noyce et al., 2006). Noyce's team,

unsurprisingly, found that pure Cu coupons completely killed three different MRSA strains in a range of 45-90 minutes at room temperature, compared to SS which did not induce a reduction in bacterial CFU (Noyce et al., 2006). In addition, they noted that Brass, consisting of 80% Cu, did result in a reduction of CFU of the various MRSA strains, though a greater time was required, and total kill was not achieved. Further, they determined that Zn was not efficacious in reducing bacterial CFU count (Noyce et al., 2006). Research on Cu as a biocidal surface is extensive and well document, with work being done to test Cu against many pathogens (Table 1).

Table 1: Contact Killing times of Pathogens on Copper Surfaces

Species	Application Method	Killing Time, RT[a]	Reference
Salmonella enterica	Wet, 4.5 × 10^6 CFU[b]	4 h	Faúndez et al., 2004
Campylobacter jejuni	Wet, 4.5 × 10^6 CFU[b]	8 h	Faúndez et al., 2004
Escherichia coli O157	Wet, (3-4) × 10^7 CFU[c]	65 min	Wilks et al., 2005

Table 1, cont.

EMRSA-1e (NCTC11939)	Wet, (1-1.9) × 10^7 CFU[c]	60 min	Noyce et al., 2006
EMRSA-16e (NCTC13143)	Wet, (1-1.9) × 10^5 CFU[c]	90 min	Noyce et al., 2006
Listeria monocytogenes Scott A	Wet, 10^7 CFU[c]	60 min	Wilks et al., 2006
Mycobacterium tuberculosis	Wet, 2.5 × 10^7 CFU[f]	5 to 15 days[g]	Mehtar et al., 2008
Candida albicans	Wet, >10^5 CFU[f]	60 min	Mehtar et al., 2008
Klebsiella pneumoniae	Wet, >10^7 CFU[f]	60 min	Mehtar et al., 2008
Pseudomonas aeruginosa	Wet, >10^7 CFU[f]	180 min	Mehtar et al., 2008
Acinetobacter baumannii	Wet, >10^7 CFU[f]	180 min	Mehtar et al., 2008
MRSA	Wet, >10^7 CFU[f]	180 min	Mehtar et al., 2008
Influenza A virus (H1N1)	Wet, 5 × 10^5 viruses[h]	6 h, 4-log decrease	Noyce et al., 2007
C. difficile (ATCC 9689) vegetative cells and spores	Wet, 2.2 × 10^5 CFU[c]	24-48 h	Weaver et al., 2008
C. difficile NCTC11204/R20291 vegetative cells	Wet, (1-5) × 10^6 CFU[i]	30 min	Wheeldon et al., 2008

Table 1, cont.

C. difficile dormant spores	Wet, 8×10^6 CFU[i]	Unaffected in 3 h	Wheeldon et al., 2008
C. difficile germinating spores	Wet, 8×10^6 CFU[i]	3 h, 3-log decrease	Wheeldon et al., 2008
Pseudomonas aeruginosa PAO1	Wet, 2.2×10^7 CFU[j]	120 min	Elguindi et al., 2009
MRSA NCTC 10442	Wet, 2×10^7 CFU	75 min, 7 log decrease	Michels and Noyce, 2009
Escherichia coli W3110	Dry, 10^9 CFU[i]	1 min	Sun et al., 2006
Acinetobacter johnsonii DSM6963	Dry, 10^9 CFU[k]	A few minutes	Santo et al., 2010
Pantoea stewartii DSM30176	Dry, 10^9 CFU[i]	1 min	Santo et al., 2010
Pseudomonas oleovorans DSM 1045	Dry, 10^9 CFU[k]	1 min	Santo et al., 2010
Staphylococcus warnerii DSM20316	Dry, 10^9 CFU[k]	A few minutes	Santo et al., 2010
Brachybacterium conglomeratum DSM 10241	Dry, 10^9 CFU[k]	A few minutes	Santo et al., 2010

Table 1, cont.

Aspergillus flavus	Wet, (2-300) × 10^5 spores[c]	120 h	Weaver et al., 2010
Aspergillus fumigatus	Wet, (2-300) × 10^5 spores[c]	>120 h	Weaver et al., 2010
Aspergillus niger	Wet, (2-300) × 10^5 spores[c]	> 576 h	Weaver et al., 2010
Fusarium culmonium	Wet, (2-300) × 10^5 spores[c]	24 h	Weaver et al., 2010
Fusarium oxysporum	Wet, (2-300) × 10^5 spores[c]	24 h	Weaver et al., 2010
Fusarium solani	Wet, (2-300) × 10^5 spores[c]	24 h	Weaver et al., 2010
Penicillium crysogenum	Wet, (2-300) × 10^5 spores[c]	24 h	Weaver et al., 2010
Candida albicans	Wet, (2-300) × 10^5 spores[c]	24 h	Weaver et al., 2010
Enterococcus hirae ATCC 9790	Wet, 10^7 CFU[c]	90 min	Molteni et al., 2010
Different Enterococcus spp.	Wet, 10^6 CFU[f]	60 min	Warnes et al., 2010

Table 1, cont.

Candida albicans	Dry, 10^6 CFU[k]	5 min	Quaranta et al., 2011
Saccharomyces cerevisiae	Dry, 10^6 CFU[k]	30 s	Quaranta et al., 2011

Interestingly, in 2020 during the Covid-19 pandemic, Mantlo et al. identified that a copper iodine complex was effective in reducing the viral titer of SARS-CoV-2. Clyraguard (Clyra Medical Technologies), is a copper iodine complex approced by the FDA, intended for use as a decontaminating agent for PPE. Further, it is cleared for use on skin and in wounds which is remarkable because normally, iodine products such as Lugol's and PVP-1 cause skin sensitivity, staining, and generally present with toxicity concerns (Mantlo et al., 2020). That said, iodine has been shown to have antiviral activity, specifically against modified vaccinia virus (MVA), MERS-CoV, influenza A virus, poliovirus type 1, and adenovirus type 3 (Eggers et al., 2015; Wada et al., 2016). Mantlo's team tested the copper iodide (undiluted 90 µl), 1:10, and 1:100 dilutions with sterile saline against SARS-CoV-2 using a Vero cell monolayer infection model. Aliquots of the virus (10 µl), were used to test each concentration, followed by incubation for 30 seconds, 10, 30, and 60 minutes at room temperature; whereafter the viral titers were determined by $TCID_{50}$ in 96-well plates. The undiluted copper iodine complex was able to significantly reduce viral titers after 10 minutes of incubation (p-value <0.0001), and after 30 and 60 minutes of exposure, the viral titer fell below the detection limit (< 75 $TCID_{50}$ per ml). It should be noted however, that the diluted concentrations were unable to inactivate SARS-CoV-2 at any length of time (Mantlo et al., 2020). It should also be noted that the copper iodine complex that displayed antiviral activity has

also been tested on several bacterial, of which include Enterococcus faecium, Staphylococcus aureus, Klebsiella pneumoniae, *Acinetobacter baumanii, Pseudomonas aeruginosa, Enterobacter aerogene,* and *Bacillus fragillus* where it was found to be effective for up to 72 hours (Mantlo et al., 2020).

2.4 Magnetic Nanoparticles

Magnetic NPs have been increasingly used in the biomedical field for a range of applications such as site-specific drug delivery, bacterial sensing for diagnosis, and magnetic hyperthermia (Hajalilou et al., 2021; Rezanezhad et al., 2021), and MRI imaging contrast (Estelrich et al., 2015). Moreover, iron oxide NPs are one of the only FDA-approved nanomaterials for cancer therapy/diagnosis, and for the treatment of iron deficiency anemia via liposomal drugs (Soetaert et al., 2020). At or below the critical size of ≈50 nm, iron oxide NPs, already having a high magnetic saturation, present with a unique magnetic form termed the superparamagnetic state (Ohannesian et al., 2019). The superparamagnetic state is possible because at or below the critical size of 50nm, behave as single-domain particles, that is, each particle behaves as though it is comprised of a single magnetic moment. In contrast, bulk Fe3O4, the ferromagnetic form, is comprised of many magnetic moments. Thus, superparamagnetic iron oxide nanoparticles (SPIONs), have a zero-net magnetization in the absence of a magnetic field due to the random ordering of the billions of particles (Ohannesian et al., 2019). In addition, other benefits of utilizing SPIONs in biomedical approaches is that they lack toxicity, are synthesized with relative ease, and can be recycled via biochemical pathways involved in iron metabolism or excreted. Iron oxides, both γ-Fe2O3 and Fe3O4 (the most commonly used in biomedical applications), are subject to leeching in acidic environments, such as tumor microenvironments, but this can be circumvented via a variety of surface coatings. In addition, SPIONs are also

subject to elimination via the reticuloendothelial system, making them useful for imaging all throughout the body. The application that has been increasingly studied, as it shows promise for aiding in cancer treatment, is magnetic hyperthermia (Hajalilou et al., 2021; Rezanezhad, 2021).

2.5 Heating Mechanism of Magnetic Nanoparticles

The main reason SPIONs are ideal for magnetically induced hyperthermia, is that, in an alternating magnetic field, SPIONs generate heat by converting magnetic power into thermal energy. Hysteresis, Brownian, and Neel losses are the dominant heat generation mechanisms of magnetic NPs (MNPs) (Martirosyan, 2012). Transformation of magnetic power into thermal energy by hysteresis loss occurs due to the hysteretic properties of ferromagnetic materials, and is a measure of the dissipated energy in the form of heat during each cycle of magnetization and reversal (Bertotti, 1998). Accordingly, hysteresis loss is highly dependent on the strength of the alternating magnetic field (AMF). However, hysteresis loss is more common in multi-domain particles in which the many domains, as they align their spin with the AMF, lose magnetic power as heat (Blundell, 2011). In contrast, single-domain NPs, such as SPIONs, experience little hysteresis loss, due to decreasing amounts of magnetic domains that reflects decreasing particle size (Martirosyan, 2012).

The Neel loss heat generation mechanism occurs because the magnetic moments of the MNPs constantly re-orient themselves to align with the AMF, and as they return to their preferred orientation, they release energy in the form of heat. In Neel loss, because it is the magnetic moments themselves that are switching their axes (Figure 5), the physical orientation of the particles are unaffected because the AMF is oscillating very rapidly. Thus, Neel loss is one of the dominant mechanism in single domain MNPs, and is inversely proportional to the size of the

MNPs because less energy is requires to change the direction of the magnetic moment than the entire particle. Neel relaxation time (τ_N) can be defined as (Neel, 1952; Brown, 1963) in Eq. (1):

$$\tau_N = \frac{\tau_0}{2}\sqrt{\pi\frac{k_B T}{kv}}e^{K\,V}/_{k_B T} \qquad (1)$$

where K is the anisotropy of the MNP, T is the temperature, K_B is the Boltzmann constant, and V is volume of the MNP. The other dominant form of heat generation for single-domain MNPs such as SPIONs, is Brownian loss. Brownian loss refers to heat generation from friction as the particle creates shear stress in its medium as the particle rotates respective to the AMF (Figure 5) Brownian relaxation time (τ_B) (Laurent et al., 2011) is defined in Eq. (2) as:

$$\tau_B = \frac{3\eta v_H}{k_B T} \qquad (2)$$

where VH is the hydrodynamic volume of the MNP, and η is the liquid mediums viscosity (Laurent et al., 2011). To understand how both Neel and Brownian loss contribute to heat generation in magnetic hyperthermia, we can define the effective time (τ) with Eq. (3):

$$\frac{1}{\tau} = \frac{1}{\tau_B} + \frac{1}{\tau_N} \qquad (3)$$

With this time constant, we can determine how heat is dissipated with MNPs. Should an AMF be made to oscillate faster than the relaxation times of the MNP, thermal energy will be released due to the delay in relaxation of the magnetic moment (Laurent et al., 2011).

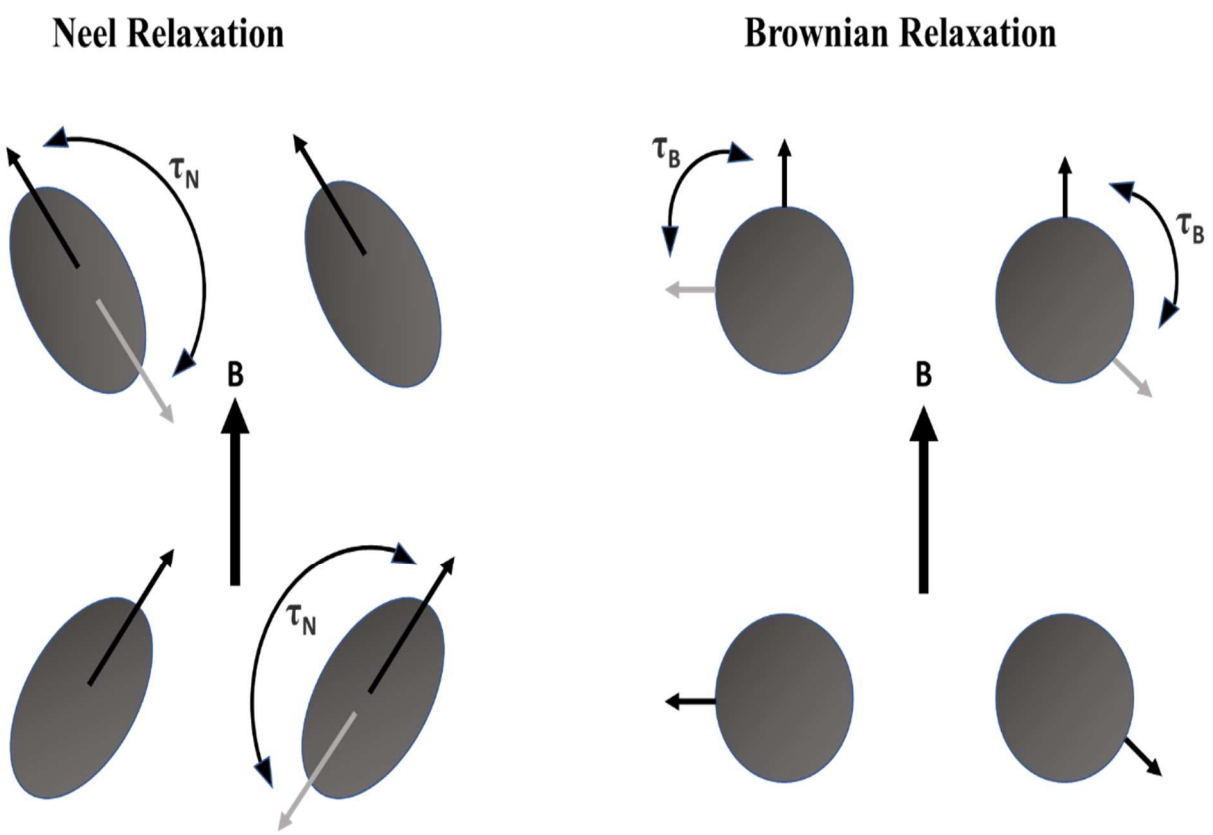

Figure 5: Neel and Brownian Relaxation

Above in figure 5, Neel and Brownian relaxation visualized as heating mechanism of SPIONs. B is the direction of the magnetic field, τ_B and τ_N represent the physical re-orientation and shift in axis of the magnetic domain, respectively.

2.6 Specific Power Absorption and Effect of Heat on Cells

To further understand how MNPs can be applied for magnetic hyperthermia, the power dissipation must be accurately quantified, because heating cancerous tissue presents with the risk of overheating healthy tissue as well. To quantify power dissipation, we use specific power absorption (SPA), measured in Wg^{-1}. The SPIONs heating efficiency is characterized by their specific power absorption rate (SAR) or specific power loss (SLP) which is a parameter defined by the thermal power per mass of the magnetic material that is generated in an AC magnetic

field. More specifically, SAR is largely dependent on which carrier fluid is used as the heat capacity and viscosity can vary, along with the frequency (f) and amplitude (H) of the magnetic field, as well as the size, shape, and concentration of the SPIONs (Hajalilou et al., 2021). The SAR can be defined by Eq. (4) as:

$$SPA = [\frac{m_{LIQ}C_{LIQ}+m_{NP}C_{NP}}{m_{Np}}](\frac{\Delta T}{\Delta t}) \qquad (4)$$

where m_{LIQ} and C_{LIQ} define the mass and heat capacity, respectively, of the medium the MNPs are suspended, and m_{NP} and C_{NP} are the MNPs mass and heat capacity. In addition, $(\frac{\Delta T}{\Delta t})$ represents the rate at which the temperature is elevated (Goya et al., 2013). However, since the mass and heat capacity of the MNPs can be considered negligible, the Eq. (5) then becomes:

$$SPA = [\frac{m_{LIQ}C_{LIQ}}{m_{Np}}](\frac{\Delta T}{\Delta t}) \qquad (5)$$

Further, the magnetic field f and H have an upper limit when considering magnetic hyperthermia as a treatment, since the human body is subject to nerve stimulation, and effects from the electromagnetic field (Rezanezhad et al., 2021; Hergt and Dutz, 2007). For reference, the product of the magnetic fields f and H should be less than 5×10^9 $Am^{-1}s^{-1}$ to get the optimum combination of f and H for maximized SLP, when considering the biomedical effects of prolonged exposure to an alternating magnetic field (Hergt and Dutz, 2007). It is important to consider all parameters for magnetic hyperthermia treatment, because optimization of the SLP is necessary for ensuring targeted treatment while minimizing any non-selective heating of neighboring healthy tissue. Another parameter that should be considered when discussing magnetic hyperthermia for cancer treatment is the thermal dose. The thermal dose determines

how much heat should be applied and for how long in a given tissue. In 1980, Dickson and Calderwood recognized, with then novel research, that "thermal death time," the time required for destruction of living tissue at a certain temperature, varied from normal tissue to tumors. It was apparent that at 42 °C, there is selective and irreversible metabolism inhibition in several rodent, human, and rabbit tumors (Dickson and Calderwood, 1980). In addition, the inhibition of metabolism of the tumor cells is associated with a loss of malignancy, while normal healthy tissues did not experience any changes in metabolism. While it was observed that above 42 °C, metabolism inhibition was more rapid in tumor cells, the healthy tissues also experienced inhibition at prolonged times, thus heating should not exceed 45 °C for prolonged times (Dickson and Calderwood, 1980). Thus, it is important to accurately characterize the thermal dose, so as to ensure quantities of heat intolerable to healthy tissues are not reached (Martirosyan, 2012). Thermal damage that tissues experience is dependent on the tissue sensitivity, as well as the temperature and time of exposure. Moreover, while tissue sensitivity can vary greatly among different tissues, it is recognized that there is a "breakpoint" in cell death rate at temperatures near 43 °C (van Rhoon et al., 2013). This temperature, 43 °C, was thus used to model the thermal dose, allowing for the conversion of a time-temperature history into an equivalent time frame for heating at the temperature 43 °C (van Rhoon et al., 2013). The thermal dose is defined by Eq. (6):

$$CEM43^0C = \sum_{i=1}^{n} t_i R^{(43-Ti)} \qquad (6)$$

where CEM43 °C represents the cumulative time in equivalent minutes at 43 °C, t_i stands for the "i-th" interval, R relates temperature dependence of cell death rate, and T is the average temperature during the time interval. The CEM43°C thus dictates the effect that the duration of

heating has on cell death (van Rhoon et al., 2013). Heat, of temperatures of roughly 45 °C, is a desirable moiety of treatment for cancer, because heat induces cell death in a repetitious and predictable manner. Further, treatment with heat, i.e. hyperthermia, is useful because cells that have a low pH, are nutritionally depleted, or are in the S-phase are more sensitive to heat than others, take cancer cells for example. In addition, heat is weakly mutagenic meaning little risk is involved in terms of conferring further mutations to existing cancer cells when employing heat as a treatment modality (Hall et al., 1984).

In fact heat shock, by means of hyperthermia, while being highly complex, is one of the most studied stress factors. Most cellular components and metabolic processes are involved in a cell's response to heat stress (Kantidze et al., 2016). In addition, it is documented that exposure to heat stress results in cells having an increase in sensitivity to factors that cause double-stranded DNA breaks (DSBs), i.e., ionizing radiation. Increased sensitization to radiotherapy by means of heat stress is termed "heat radiosensitization" (Iliakis et al., 2008). Further, heat stress has been shown to induce DNA damage in addition to inhibiting nearly all DNA repair systems (Kantidze et al., 2016). For example, base excision repair (BER), nucleotide excision repair (NER), non-homologous DNA end joining (NHEJ), and homologous recombination (HR) are inhibited by heat stress (Kantidze et al., 2016). More specifically, heat stress inhibits DNA repair, thereby increasing radiosensitization, by causing misfolding and aggregration of important enzymes involved in the systems, such as DNA-dependent protein kinase (DNA-PK) in NHEJ, or DNA glycosylases involved in base excision repair (Dikomey et al., 1987). Thus, hyperthermia, as a result of directly inhibiting various DNA repair pathways, increases the efficacy of radio- and chemotherapy for anti-cancer treatments (Eppink et al., 2012). Aside from protein folding and aggregation, exposure of the hydrophobic chemical groups that make up proteins can also leads to improper protein

interactions that lead to cellular destruction (Eppink et al., 2012). Double stranded breaks (DSBs), since they can result in rearrangements of the genome, are especially dangerous. Although they can arise normally during the cell life cycle, mis-repair can lead to carcinogenesis. Alternatively, DSBs can also lead to apoptosis, a phenomenon that can be exploited in anti-cancer treatments. Hence, hyperthermia used in conjunction with radio- or chemotherapy, increases treatment efficacy by preventing cancerous or damaged cells from healing via DNA repair pathways, effectively sensitizing cells to treatments that induce DNA damage (Eppink et al., 2012). Accordingly, magnetically induced hyperthermia has been studied as a promising method of aiding in current cancer therapies and can be achieved via various methods. Hyperthermia as a treatment is attractive because it comes with less restrictive side effects than traditional cancer treatments like radiotherapy and chemotherapy, while also having the potential to be used alongside them (Moroz et al., 2002). Hyperthermia, in the context of cancer treatment, is defined as having a mean body temperature higher than normal (Jha et al., 2016), and can be classified as local, regional, and whole-body heating (NIH, 2021). Whole-body hyperthermia is achieved by wrapping the patient in hot blankets or placing them in a thermal chamber to reach a temperature of 42-43 °C for a short time, while regional hyperthermia focuses on areas of the body, such as entire organs or limbs (NIH, 2021). In localized hyperthermia, physicians and researchers only apply heat to specific areas, generally directly at or near sites at which the tumor is located (NIH, 2021). In one form of treatment, SPION-based ferrofluids are directly injected to the tumor environment where an alternating magnetic field can be applied to induce magnetic hyperthermia, heating the tumor microenvironment from 37 °C to 45 °C (Hajalilou et al., 2021; Rezanezhad et al., 2021). While the results were promising with the MNPs showing tumor shrinkage, hyperthermia treatment can be further enhanced by modification of their surface with surfactants of desired biomolecules.

Organic and inorganic surfactants both play a role in varying the colloidal stability, biocompatibility, and attraction toward specific target molecules.

2.7 Modification of SPIONs for Improving Biomedical Applications

Part of this chapter have been published in Future Medicinal Chemistry, Vol. 13, No. 21 (Arriaga et al., 2021). Silverio A. Lopez conducted alternating magnetic-induced hyperthermia and assisted in electron microscopy to help determine how varying wt. %'s of SPIONs would affect the achieved temperatures.

Although iron oxide NPs are biocompatible at low doses, toxicity limits prevent large doses from being uses; however, this can be circumvented via biocompatible composites, polymers, and ceramics. Through using more biocompatible surface coatings, NPs can be made less or nontoxic. Further, surface coatings reduce unwanted premature reactions between the body and the NPs while also reducing particle aggregation (Mondal et al., 2017). Further still, coatings can offer the advantage of serving as a matrices for drugs, biomolecules, or other NPs to improve their delivery to the target site (Figure 6). Such coatings are employed based on the desired applications, in example, anticancer treatment, imaging, or drug-delivery. For example, in anticancer treatments such as magnetic hyperthermia, the goal would be to improve the magnetic properties, NP delivery, biocompatibility, and uptake into the cancer cells. To improve the colloidal stability of NPs and prevent their agglomeration in solution, surfactants such as dextran have been utilized. Surfactants provide a long enough intermolecular distance that the NPs do not agglomerate and can control help tune particle size during the synthesis process (Ohannesian et al., 2019). To further that point, Tseng et al. conjugated dextran-coated SPIONs with cetuximab, a monoclonal antibody. Cetuximab (C225, Erbitux®), a chimeric murine/human monoclonal antibody, targets human

EGFR specifically (Tseng et al., 2015). Cetuximab has been approved for "[first-line treatment against K-ras wild-type EGFR-expressing metastatic colorectal cancer]" and the researchers successfully demonstrated that their cetuximab conjugated SPIONs inhibited EGFR degradation and internalization as well as increased apoptosis in EGFR-expressing tumor cells (Tseng et al., 2015). In addition, they noted that there was an increase in receptor-mediated endocytosis of the SPIONs which suggests potential for both treatment and concurrent imaging of the target site.

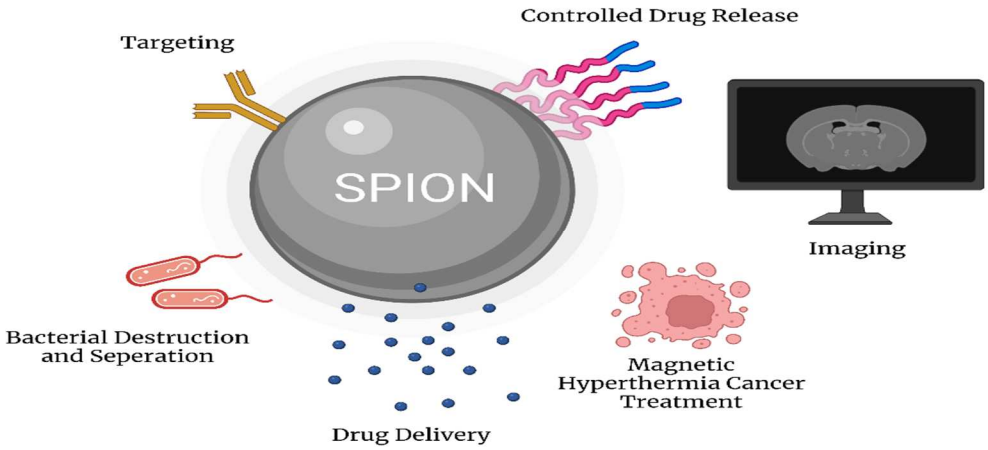

Figure 6: SPION modified for various biomedical applications

In this study, Arriaga et al. evaluated the ability of varying weight percent's of SPIONs to control the release-rate of minocycline from a PLGA scaffold via magnetic hyperthermia. In addition, they evaluated the cytotoxicity of Fe3O4 SPIONs via an MTT Assay (Figure 7) testing 0.001, 0.002, 0.005, 0.0075, 0.010, 0.0125, 0.015, and 0.02 g/mL at 37◦C to determine viability of U-87 MG glioblastoma cells. At max dose, the U-87 glioblastoma cells were exposed to an amount of Fe3O4 SPIONs that would be equal to that of a 20 wt. % NP scaffold, and it was shown that

there was no significant difference in cell viability of any dose of Fe3O4 SPIONs from the control (Figure 7).

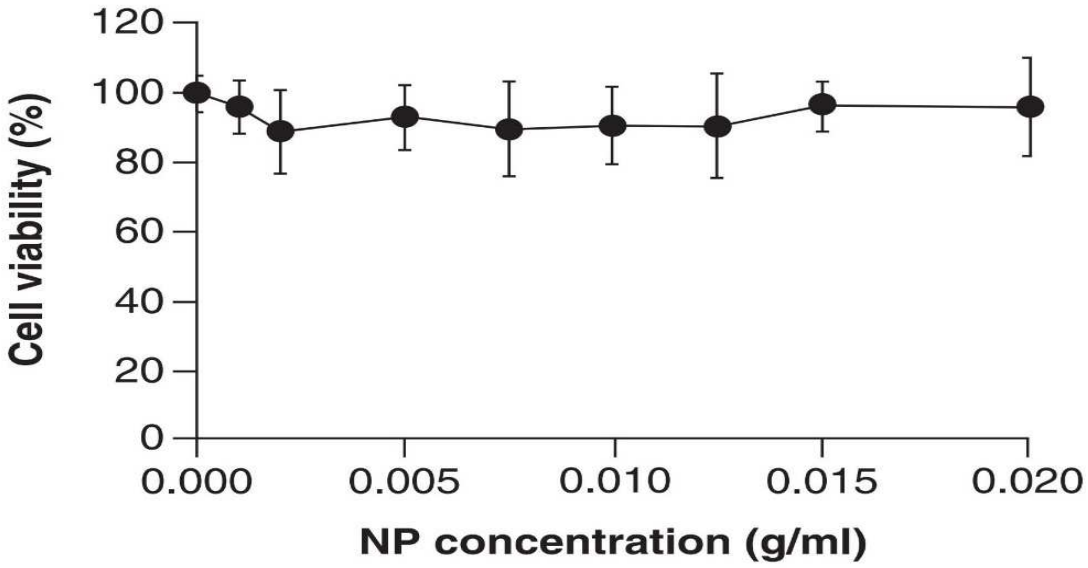

Figure 7: Cell viability for U87 cells treated with different concentrations of Fe3O4 NPs

Arriaga et al. then looked at how elevated temperatures (42 ◦C) versus normal physiological temperature (37 ◦C) effected minocycline release from the PLGA scaffold (Figure 8). For the scaffolds exposed to 37 ◦C, 4.8 ± 3.1%, 5.3 ± 2.9% and 5.8 ± 3.0% of drug was released at 20, 40 and 60 min, respectively; while the scaffolds exposed to 42 ◦C, 11.1 ± 2.2%, 16.5 ± 6.1% and 18.8 ± 5.8% of drug was released at 20, 40 and 60 min, respectively. After 40 minutes, it was observed that total cumulative drug % release was greater for the scaffolds exposed to 42 ◦C than those exposed to 37 ◦C. Thus, utilizing Fe3O4 SPIONs in increasing wt %'s (Figure 9) would allow for controlling the release rate of minocycline from the PLGA scaffold by varying the temperature induced by magnetic hyperthermia.

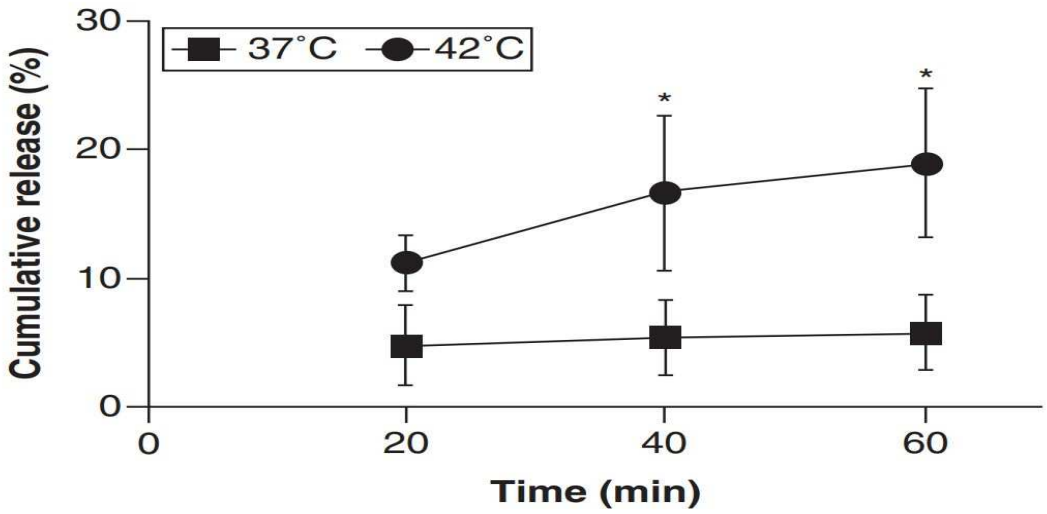

Figure 8: Cumulative drug release (%) of PLGA scaffolds fabricated with minocycline placed at 37 versus 42◦C

PLGA scaffolds with varying wt. % amounts of Fe3O4 SPIONs were then tested in an alternating magnetic field, to determine the SPIONs ability to generate heat. Using a nanoscale Biomagnetisc DM100 Calorimeter (nanoScale Biomagnetics, Spain), a frequency of 604 kHz and magnetic field of 300 Oe was produced to cause heating, which was measured with a fiber optic probe (Arriaga et al., 2021). In the test, the starting temperaute was ~22–24◦C (room temperature), with the goal temperauture being an increase of 5 ◦C. Note that physiological temperature would be 37 ◦C, with a 5 ◦C increase resulting in a 42 ◦C, the desired treatment temperature. The results of the test are shown in figure 9. After 20 min, the scaffolds with 5, 10 and 15 wt. % achieved an increased in temperature of 4.7, 5.8 and 6.8◦C, respectively. Then, at 40 min, the scaffolds produced with 5, 10 and 15 wt. % achieved an increased in temperature of 6.6, 8.4 and 9.5◦C, respectively. After 60 min, the scaffolds produced with 5, 10 and 15 wt. % achieved an increased in temperature of 7.4, 9.5 and 10.5◦C, respectively. The scaffolds fabricated with 5, 10 and 15 wt. % took 22.1, 15.3 and 13.3 min, respectively, to achieve an increase of temperature of 5◦C.

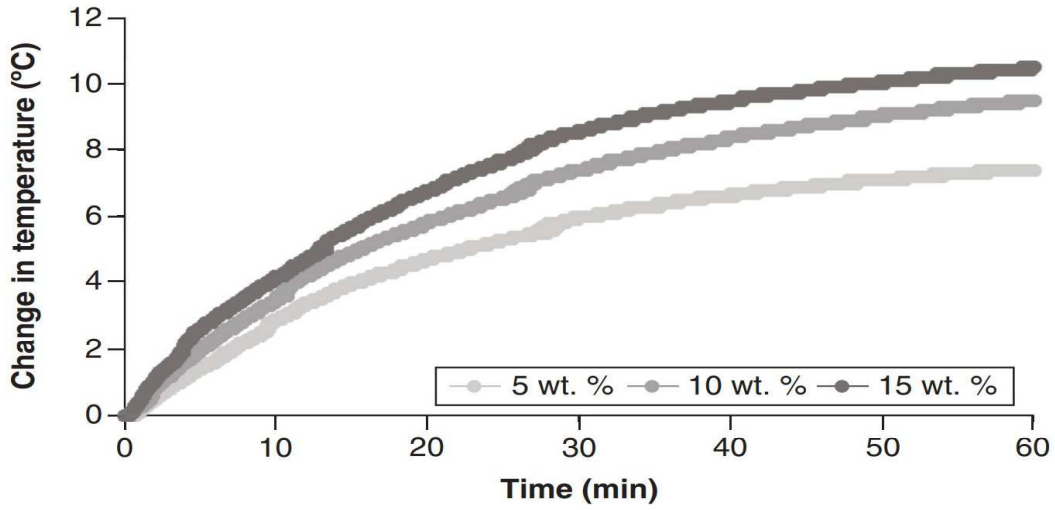

Figure 9: Change in temperature over 60 min for PLGA scaffolds made with minocycline and different wt. % of Fe3O4 nanoparticles.

After it was found that the addition of SPIONs in to the PLGA scaffold could produce sufficient temperature changes (ie. 5◦C), U87-MG glioblastoma cells were exposed to 37◦C or 42◦C with and without minocycline to ascertain their viabilities following treatment (Figure 10). The cells exposed to 37◦C without drug were used as controls, having 100% viability. Cells exposed to minocycline at either temperature are denoted as '37M' and '42M' and had cell viabilities of 85.6% and 54.5%; both of which, were significantly lower than the control. Alternatively, the cells exposed to 42 ◦C without minocycline had a viability of 89%, and as such were not significantly different from the control (Arriaga et al., 2021).

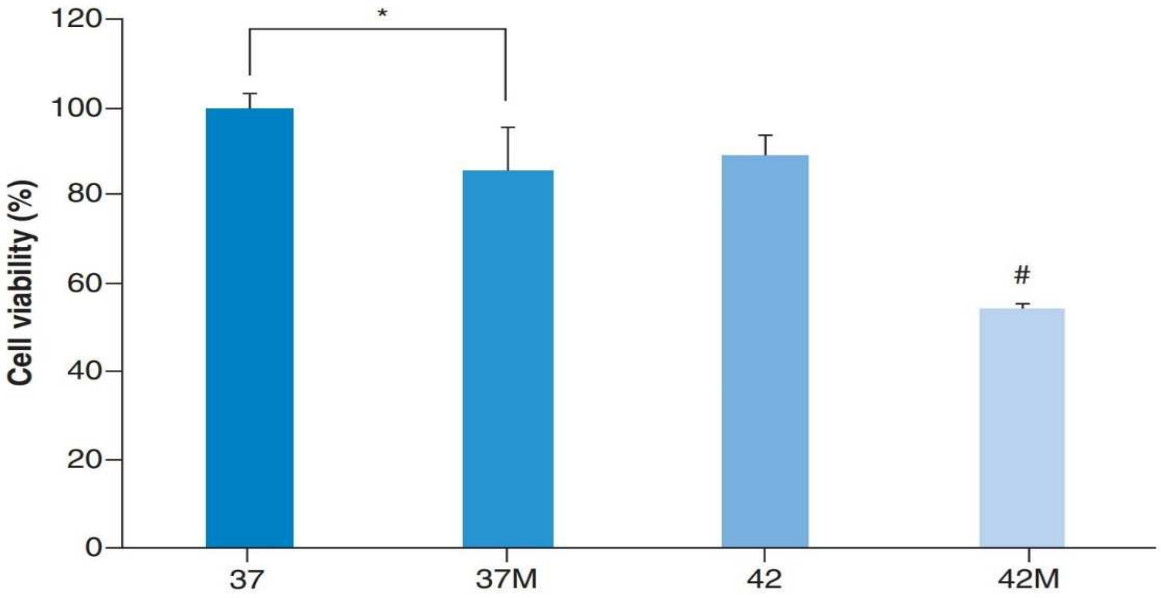

Figure 10: Cell viability of U87-MG glioblastoma cells exposed to elevated temperatures

Overall, Arriaga et al. were able to show that Fe3O4 SPIONs are capable of being used to control the release rate of minocycline from a PLGA scaffold by varying the wt% incorporated into the scaffold. Further, their findings showed that the elevated temperatures produced due to magnetic induced hyperthermia can work synergistically with minocycline to enhance glioblastoma cell death.

Despite great attention to tuning the size, surface coating, and magnetic properties of ferrite based MNPs, their magnetic capabilities and heating capabilities are limited in vivo (Nemati et al., 2017). In addition, its been reported that varying the shape of the MNPs leads to improvements in the SAR by altering shape anisotropy. In example, nano-octopods, nanocubes, nanorods, and MNPs designed to resemble bacterial magnetosomes have all been reported to improve the SAR for heat generation (Nemati et al., 2016; 2018; Nikiin et al., 2019; Martinez-Boubeta et al., 2013). More recently, MNPs based on cobalt (Co) ferrite have been gaining an increasing amount of

attention, as they have high magnetic crystalline anisotropy, Curie temperature, and an intermediate magnetization saturation at relatively small particle sizes (Kathickraja et al., 2019). For those reasons, cobalt ferrite MNPs would mean a smaller therapeutic dose would be required for magnetic hyperthermia, especially when considering how size, shape, and surface coatings can improve the desired properties. Using a two-step hydrothermal process, Kathickraja et al. were able to procuce CoFe2O4 NPs encased in a rod-like hydroxyapatite structure, which, upon heat treatment, resulted in core-shell nanostructured CoFe2O4@Hap NPs. The core-shell CoFe2O4@Hap NPs then had there cytotoxicity on fibroblast 3T3 tested using an MTT assay, whereupon they found that when incubated at a high concentration(500 μg ml^{-1}) for 24 hr, more than 76% of the cells retained their viability, indicating low cytotoxicity, while lower concentrations (400 μg ml^{-1}), cell viability was as high as 100% (Kathickraja et al., 2019). Thus, they were able to produce magnetic NPs with enhanced magnetic properties compared to Fe3O4 based NPs, while still displaying high biocompatibility. Thus, SPIONs on their own can be used as a cancer treatment, while also offering synergistic effects with chemo- and radiotherapies; further being improved by modification with surfactants, other ferromagnetic materials, and biological molecules.

CHAPTER III

MATERIALS AND METHODS

3.1 Preparation of (10Al+3I2O5)-n wt% (2Al-3CuO) Nanothermite Mixtures

Commercially available Iodine pentoxide microparticles of 98% purity (Sigma Aldrich) were purchased to produce I2O5 nano-rod structures. Using a High Energy Shimmy Ball Mill (HSF-3, MTI Co.), I2O5 nano-rods ranging from 50-100 nm in diameter and 600 nm in length were produced (Hobosyan and Martirosyan, 2017). Copper (II) Oxide (CuO) particles with an average size of 6 mm were purchased (Sigma Aldrich) as well as nanoscale Aluminum with an average size of 100 nm (Sigma Aldrich) to prepare the nanoenergetic mixtures. For each NM, the I2O5 and CuO were mixed with the aluminum nanoparticles at the appropriate stoichiometric ratios to produce a Cu rich (Al-75%CuO-25%I2O5), 50-50 (Al-50%CuO-50%I2O5), and I rich (Al-25%CuO-75%I2O5), keeping in mind the oxidized aluminum layer on the outer surface of the aluminum nanoparticles (4-5 nm in thickness). A 3:7 ratio was used (fuel rich) as it has been determined experimentally that a fuel rich mixture produces the highest-pressure discharge value (Hobosyan and Martirosyan, 2017). Each nanoenergetic mixture was created by weighing the corresponding amounts of each reagent for the varying wt % mixtures and mixing them under a hexane environment via rotary ball milling (container volume 60cm^3). The US Stoneware rotary

ball mill was set with a rotation speed of 80 rpm for a total of 9 hours). After milling, the hexane was allowed to evaporate at room temperature, since exposing the mixture to heat could trigger a detonation, then one at a time each sample was collected.

3.2 Thermodynamic Analysis for the Al-CuO-I2O5 systems

Thermodynamic analysis of the $(10Al+3I_2O_5)$ -n wt% (2Al+3CuO) system is necessary for evaluating the energy capacity of the mixture at various composition, predicting the adiabatic temperature, condensed phase concentrations, as well as the composition and amount of gaseous products produced during the reaction. The thermodynamic estimation of the equilibrium composition of complex multicomponent multiphase systems requires minimization of the thermodynamic free energy (G) subject to mass and energy balances (Shiryaev, 1993; 1995. In addition, thermodynamic analysis can reveal the characteristics of the interphase equilibrium at different quasiequilibrium regions of the $(10Al+3I_2O_5)$ -n wt% (2Al+3CuO) system (Shiryaev, 1993). The thermodynamic calculations were performed using the 'Thermo' software (Shiryaev, 1995) in addition to the chemical computer code, 'HSC Chemistry-7' to predict the adiabatic temperature and equilibrium compositions. By taking molecular amounts of the species from the reaction and equilibrium calculation, the theoretical heat balances were calculated. By minimizing the thermodynamic potential, the composition of the equilibrium products and adiabatic temperature can be determined (Hobosyan et al., 2016). In a system with N(g) gas and N(s) solid number of components, at a constant pressure, the concentrations of the equilibrium phases can be defined by:

$$F(\{n_k\},\{n_s\}) = \sum_{k=1}^{N(g)} n_k \left(\ln \frac{p_k}{p} + G_k \right) + \sum_{l=1}^{N(s)} n_l G_l \quad (7)$$

such that p_k represents the partial pressure of the kth gas-phase component, while n_l and G_l are the number of moles and molar Gibbs free energy of the components. The adiabatic temperature of combustion, T_c^{ad}, is determined by the total energy balance defined by:

$$\sum_{i=1}^{N_0} H_i(T_0) = \sum_{k=1}^{N(g)} n_k H_k\left(T_c^{ad}\right) + \sum_{l=1}^{N(s)} n_l H_l\left(T_c^{ad}\right) \quad (8)$$

in which the enthalpy of each component is defined by:

$$H_i(T) = \Delta H_{f,i}^0 + \int_{T_0}^{T} c_{p,i} dT + \sum \Delta H_{s,i} \quad (9)$$

and $\Delta H^0_{f,i}$ represents the heat of formation at 1 atm and reference temperature T_0, $C_{p,i}$ is the heat capacity, and $\Delta H_{s,i}$ denotes the heat of the sth phase transition of the components (Arvind et al., 1998).

3.3 Pressure Discharge Testing of the Nanoenergetic mixtures

Each nano-formulation was tested to ascertain the pressure produced during detonation. For each test, 200 mg of the nanoenergetic mixtures, one at a time, were placed in a Parr Instrument High Pressure cylindrical reactor with a volume of 0.342 L and the ignition was triggered by a Ni-Cr wire. Pressure output signals were taken by a piezoelectric transducer with pressure/voltage

values (Omega) and amplified and tracked through an Omega DAQ-3005 Data Acquisition board using a signal acquisition frequency of 1MHz (Figure 11). Previous work characterizing an NM comprised of 100% Al-I2O5 (Hobosyan and Martirosyan, 2017) was also included for comparison with the novel formulations.

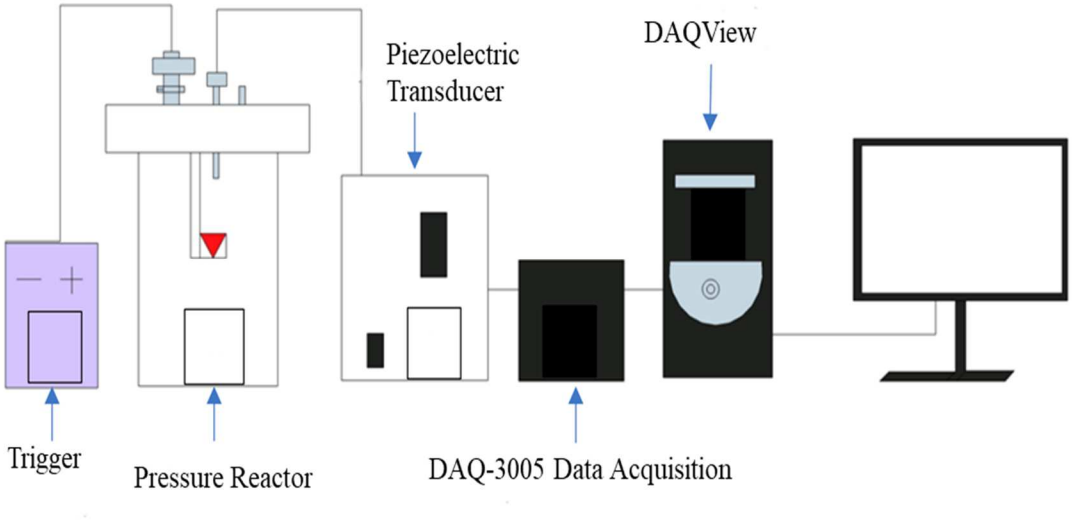

Figure 11: Pressure Discharge DAQ appartatus

3.4 X-Ray Diffraction

X-Ray diffraction (XRD) is a non-destructive technique that can be used for determining the crystal structure, particle size, studying phase equilibria, and conducting stress measurements of a sample (Echlin, 2011; Cullity, 1957). An array of diffraction maxima is obtained from XRD analysis (Klute, 1986), with which a qualitative interpretation of the diffraction patterns can be gathered. The obtained diffraction patterns are then further analyzed using 'Diffrac Suitte' as well as 'QualX' which identifies peaks and references the 'Crystallography open database' to

access thousands of known phase peaks. Following the testing that occurred within the bomb calorimeter, the product was collected from the vessel and analyzed via X-Ray diffraction to determine the phases according to their crystal structure. The XRD peaks spectra are graphed in arbitrary units to present the intensity.

3.5 Scanning Electron Microscopy and Energy Dispersive X-Ray Spectroscopy

Using a Sigma VP Field Emission Scanning Microscope, pictures were taken to analyze particle size morphology and distribution of the products formed from the NM reactions of each ratio (Echlin, 2011; Zhou et al., 2006), as well as the SPIONs produced from microfluidic-assisted synthesis. Energy dispersive X-Ray spectroscopy (EDX) is an analytical technique in which an electron beam is focused on a sample, causing an electron in the inner shell to be expulsed whereafter the 'hole' is filled by an electron from a higher energy shell. The difference in energy, which varies for each element, is then expelled as an X-Ray to the detector where it can be used to determine an element's identity, or rather, the presence of specific elements within a sample (Polini and Yang, 2017). In addition, EDX is often performed concomitantly with SEM as they both make use of an electron beam for analysis, providing both qualitative and quantitative sample analysis.

3.6 Escherichia coli and Agar Plate Preparation

To determine the biocidal efficacy of the the 50%Al-CuO–50%Al-I2O5 nano-formulation, the Escherichia coli bacteria HB101 K-12 was prepared by transferring an inoculum of E. coli from a stock vial into a tube of Luria-Bertani (LB) broth for subsequent incubation at 37 □ for several hours. The goal of incubating the E. coli was to achieve a colony forming unit (CFU) count sufficient to grow lawns from which healthy colonies could be isolated for successive testing.

While the E. coli was incubating, peptone agar was prepared to produce lawns were grown by taking the E. coli broth and streaking a zigzag pattern down the diameter of the agar plates. Distinct colonies were then used for subsequent E. coli stocks. From the stocks, further samples were grown with a large enough CFU count to perform serial dilutions. The serial dilutions were performed to result in a CFU count of 500 to distinctly quantify changes in colony count between the control and experimental plates. After serial dilutions were performed, the amount in milliliters corresponding to 180 CFU was pipetted on each 100mm plate and spread using an L-shaped spreader.

3.7 Assessing Biocidal Properties of the Nanoenergetic Mixture

Once the plates were prepared and inoculated with a calculated 180 CFU of E. coli, the experimental plates were placed within a plexiglass chamber, having a volume of 49.26 L and a wall thickness of 1.2cm at several locations (Figure 12). One plate was located directly above the charge mass (25 mg), and the others were located at each face of the chamber in an effort to ascertain how effective the 50%Al-CuO–50%Al-I2O5 NM was at dispersing the vapor, and its biocidal efficiency. The charge mass was placed at the center of the base, raised 8cm, and ignited via a variable autotransformer (Staco Energy Products). Following 1 hours of incubation, the agar plates spread with E. coli were exposed to the NM and re-introduced to the incubator where they were allowed to incubate for another 24 hours at 37 °C.

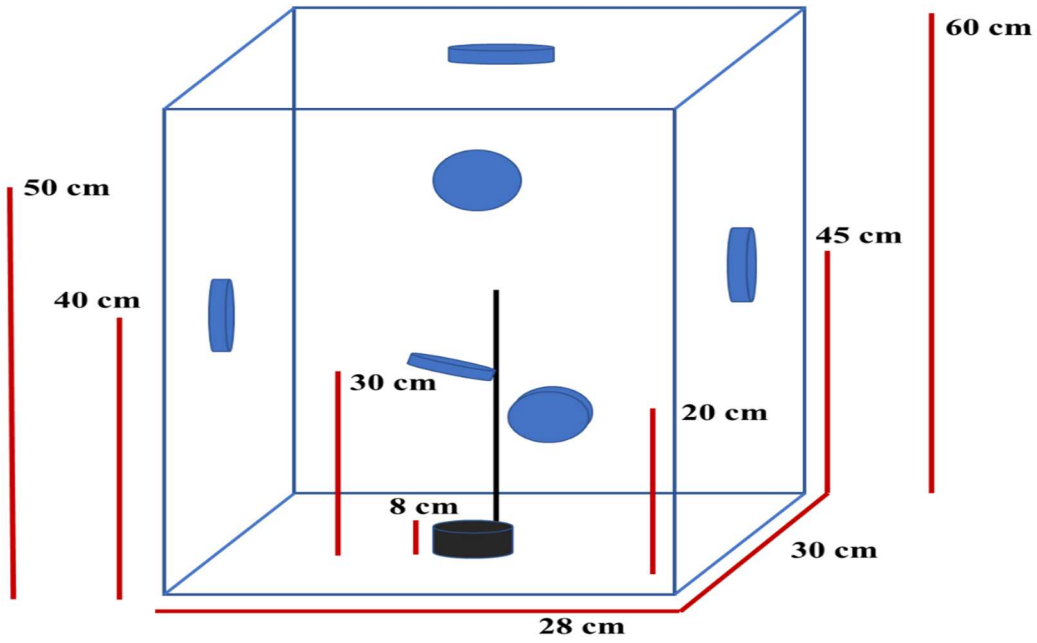

Figure 12: Illustration of the testing chamber and respective heights and orientation of each agar plate.

3.8 Microfluidic Synthesis of Dextran coated Superparamagnetic Nanoparticles

Microfluidic assisted precipitation of the dextran coated SPIONs was performed using a microfluidic pump (ISMATEC RegloICC, Peristaltic, MS-4/8). Iron II sulfate heptahydrate (FeSO4 * 7H2O), and Iron III nitrate nonahydrate (Fe(No3)3 * 9H2O) were the iron salts used in the precipitation. Dextran sourced from Leuconostoc spp., with a MW ~ 6,000, and solid Sodium hydroxide (NaOH) were also used. Polyethylene micro-tubing, diameter of 0.76mm, was used in the microfluidic system, along with a polyetheretherketone (PEEK) Y connector, diameter of 0.5mm, at which the iron salts and dextran met to interact as they passed through the remaining 60cm of polyethylene tubing. To start, the reagents are placed in separate tubes, with one tube having a mixture of the FeSO4 * 7H2O and Fe(No3)3 * 9H2O at a 1:2 molar ratio suspended in DI H2O and the other tube having the excess NaOH and 5% dextran. The dextran acts as a

surfactant, which, in addition to controlling the flow rate via the microfluidic pump, allows for tuning of the particle size. Thereafter, the tubes are filled with Nitrogen gas and 25 mL of DI H2O before they're sonicated to completely dissolve and disperse the reagents. While the reaction occurs, the reagents are constantly fed a supply of Nitrogen, 5psi, to prevent oxidation. The tubes are then connected to the microfluidic pump, set to 20 RPM, propel the reagents to the Y connector at 0.04 mL/s where they interact and nucleation begins as they pass through the collecting channel and into the collection tube (Figure 13). Following the reaction, the sample is centrifuged (LW-Scientific) at 1500 RPM to separate the product (solid phase) and waste (liquid phase) which contained the NaSO4 and NaNO3 byproducts. This washing process occurred several times, adding DI H2O each time the previous liquid phase was discarded until it remained clear following centrifugation. Thereafter, the sample was collected for characterization.

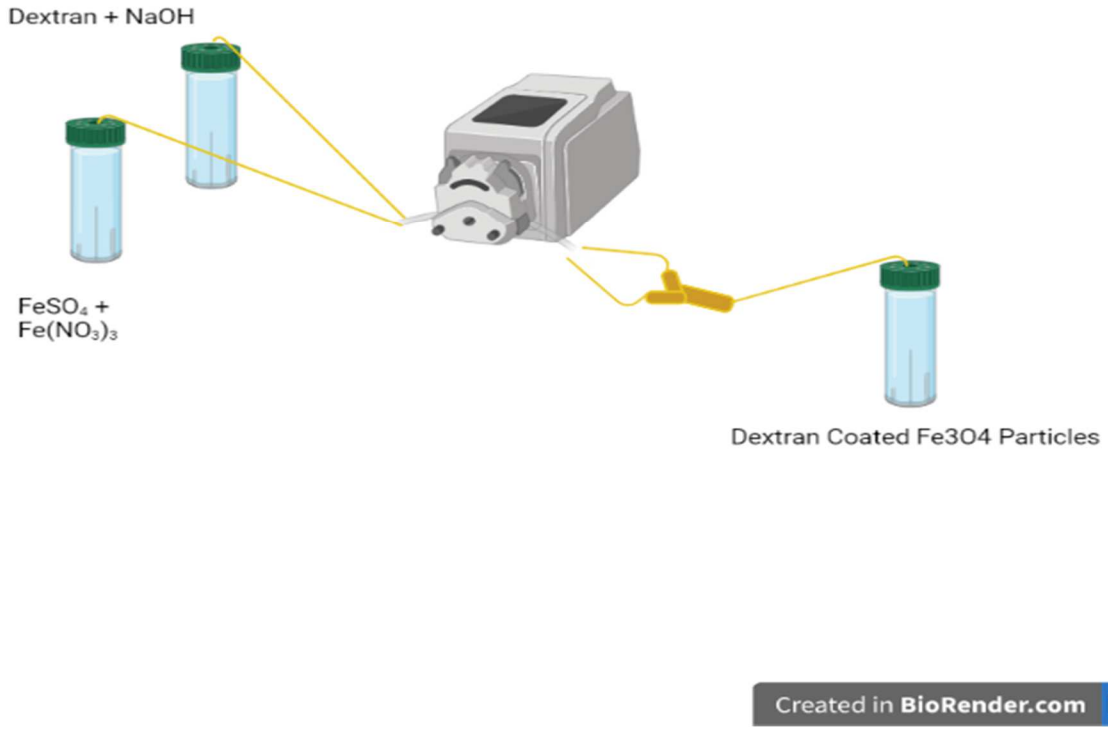

Figure 13: Graphic depicting set up of Microfluidic Assisted Synthesis of SPIONs

CHAPTER IV

FINDINGS AND DISCUSSIONS

4.1 Thermodynamic Analysis of the Al-CuO-I2O5 systems

The ($10Al+3I_2O_5$) -n wt% (2Al+3CuO) system can be observed as the interaction between the individual systems, given as:

Table 2: Independent Systems contributing to the (10Al +2I2O5) -n wt% (2Al+3CuO) Nanoenergetic systems

(1)	$10Al+3I_2O_5=5Al_2O_3+6I+\Delta H$	(–25.7 kJ/cm^3)
(2)	$2Al+3CuO=Al_2O_3+3Cu+\Delta H$	(-15.2 kJ/cm^3)

The molar ratio at which copper iodide (CuI) can be expected when combining the reactions (1) and (2) is 1:2, which correspond to 68.5 wt. % ($10Al+3I_2O_5$) vs 31.5 wt% (2Al+3CuO). Positively, the thermodynamic calculations reveal that the molar amounts of the reaction products, gaseous copper and iodine, become equal at this ratio (Figure 14). The highest adiabatic combustion temperature, 3828K, occurs when the system only contains system (1) and decreases gradually when the weight ratio of system (2) is increased. Cu and I are both in a gaseous phase at these temperatures. Keeping the system (1) mass constant and increasing the system (2) amount, the gaseous iodine concentration remains constant, while the gaseous copper amount

increases exponentially (Figure 14). At elevated temperatures, some of the liquid aluminum oxide is decomposed but this is likely due to an excess of atomic oxygen in the system. As the temperature decreases, so too does the amount of decomposed aluminum oxide with the released free oxygen nearly vanishing at about 70 wt% composition of system (2) in the mixture (Figure 14). At the 70 wt% composition of system (2), a temperature plateau occurs, at which some of the gaseous copper transition to a liquid phase (the amount is too minute to be visualized on the graph). Hence, for systems (1) and (2) to produce stoichiometric CuI in combination, 31.5 wt% of system (2) is ideal; however, as was demonstrated (Figure 15) that composition is extremely energetic and impractical for any potential industrial uses. Accordingly, the weight ratio of systems (1) and (2) selected was 50 wt% of each, as the temperature reached was in excess of 3000 K and gaseous Cu and I were predicted to form, resulting in the formation of CuI as discussed.

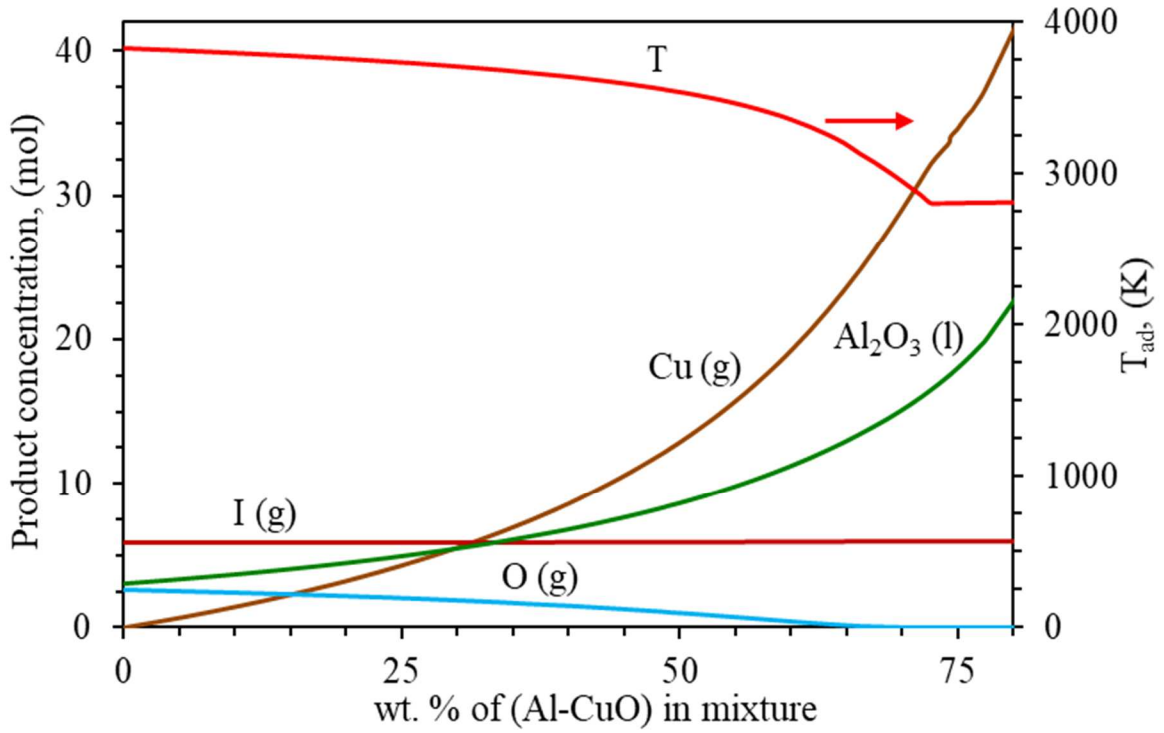

Figure 14: Adiabatic temperature of combustion and product composition dependence on the weight percentage of Al-CuO formulation in the system ($10Al+3I_2O_5$) -n wt% ($2Al+3CuO$).

4.2 Pressure Discharge values of the Nanoenergetic mixtures

Previously (Hobosyan and Martirosyan, 2017) the 100% Al-I2O5 NM had been shown to be capable of producing pressures of up to 43.4 MPa/g, and it was observed that the 25% Al-CuO – 75% Al-I2O5 nearly mirrored that, producing pressures of up to 42.5 MPa/g since I2O5 was the oxidizer present in a greater amount. Then, as the amount of both oxidizers in the NM system is changed to 50%, the pressure output significantly decreased to 9.1 MPa/g, as expected since I2O5 is responsible for more of the pressure generation (Hobosyan and Martirosyan, 2017). Further, the NM with the least wt% of I2O5, the 25%Al-CuO – 75%Al-I2O5 mixture, resulted in a pressure output of 1.7 MPa/g which is substantially lower than both systems with higher wt. %s of I2O5.

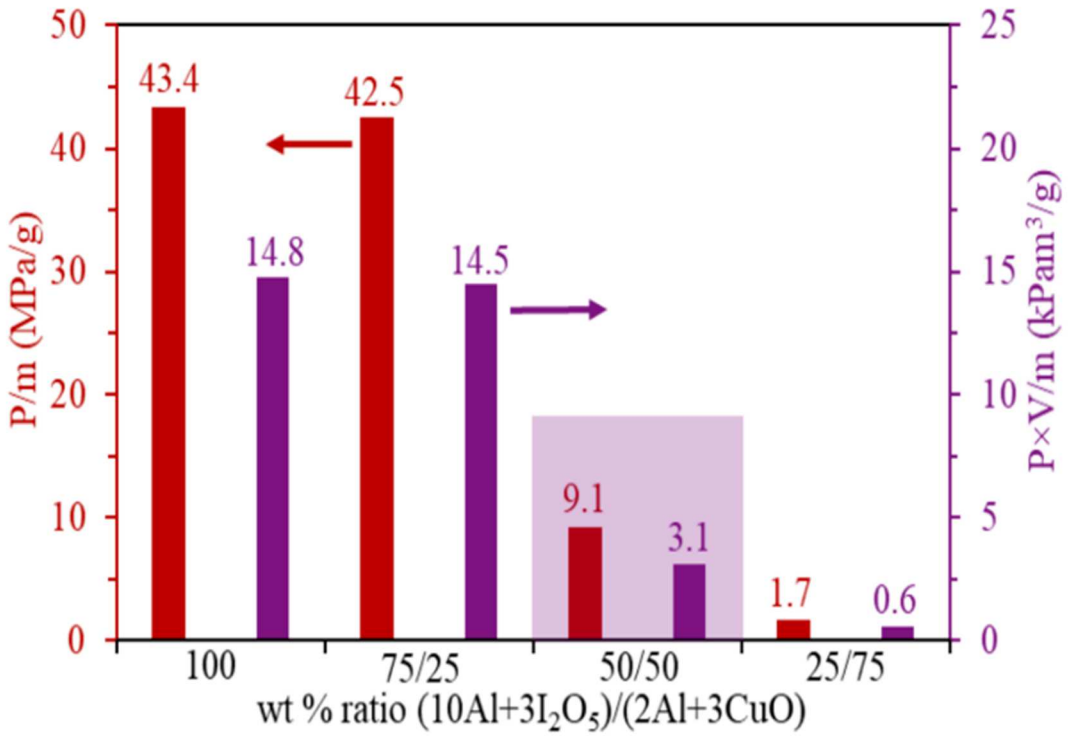

Figure 15: Pressure Discharge values of the varying wt. % ratios of the Al-CuO-I2O5 nanoenergetic systems.

4.3 Crystallinity of Al-CuO-I2O5 Reaction Product

Based on the findings from the thermodynamic analysis, it was hypothesized that CuI would be formed during the reactions due to the generation of transient gaseous iodine and copper indicated by the thermodynamic analysis, so to confirm the products' XRD spectra were compared against purchased pure copper iodine (CuI) (Figure 16). Each of the NM mixtures presented with at least 1 peak identified for CuI; however, the intensity of the peaks seems to be dependent on the ratios of the oxidizers present in the NM. The 25% Al-CuO-75% Al-I2O5 NM primarily presented with peaks for Al2O3, which correlates with the SEM images (Figure 17), since the strong initial ignition likely caused the rapid melting and cooling of Al2O3 and CuO before the CuO could interact with any vaporized I; hence the large particles in comparison to the other samples. Further, the XRD of the 75% Al-CuO-25%Al-I2O5 NM primarily presented with intense peaks for Al2O3 and CuO, which likely occurred due to the decreased amount of I2O5 resulting in less of the CuO reacting during the detonation, as this mixture of oxidizers was shown to result in a pressure generation of 1.7 MPa/g (Figure 15). In fact the EDX of the 75%Al-CuO – 25%Al-I2O5 coincides with XRD, showing that the sample was largely composed of Cu and O along with Al (Figure 16). Lastly, the 50% Al-CuO – 50% Al-I2O5 NM presented with the most intense peaks for CuI, though it should be noted that peaks for Al2O3 and CuO were present as well. The pressure discharge testing indicated that 9.1 MPa/g are capable of being produced using this ratio of oxidizers (Figure 15).

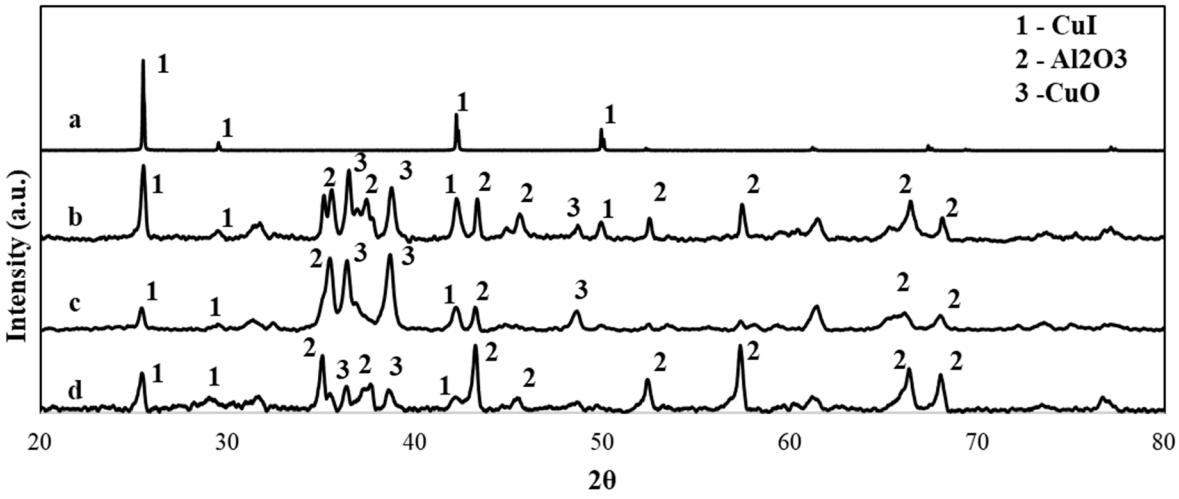

Figure 16: XRD of (A) Purchased CuI, (B) 50%Al-CuO–50%Al-I2O5, (C) 75%Al-CuO–25% Al-I2O5, and (D) 25%Al-CuO–75%Al-I2O5 .

4.4 Surface Morphology and Elemental Composition of the Nanoenergetic Systems

Scanning electron microscopy revealed that the formulation with the most I2O5, 25%Al-CuO–75%Al-I2O5, resulted in the formation of significantly larger particles (Figure 17), compared to the particles formed following detonation of both the 50%Al-CuO–50%Al-I2O5 and 75%Al-CuO–25% Al-I2O5 formulation (Figure18-19). In addition, elemental analysis indicates that the particles were primarily composed of Al and O, which correlates with the XRD findings showing intense peaks for Al2O3.

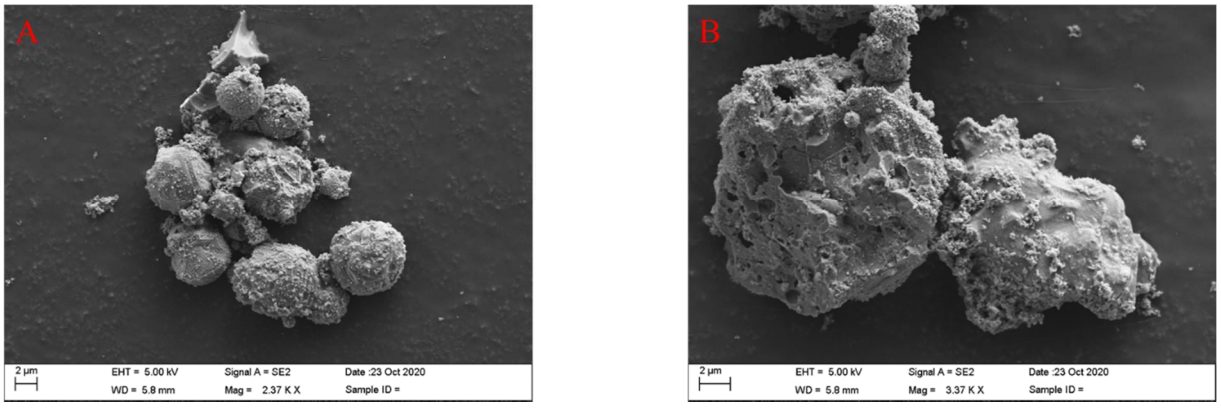

Figure 17: SEM images of the 25%Al-CuO–75%Al-I2O5 nano-formulation.

Table 3: Weight and Atomic Percent of the Al-25%CuO-75%I2O5 NM system

Element	Weight %	Atomic %	Net Int.	Error %
O	45.44	58.41	665.57	5.99
Al	54.56	41.59	532.98	6.26

The generation of particles in the micron range, from the Al-25%CuO-75%I2O5 likely resulted from a greater concentration of I2O5 the more energetic oxidizer, causing rapid melting and cooling of the Al and Cu before the gaseous Cu could condense with vaporized Iodine. The sample of the Al-25%CuO-75%I2O5 NM has both spherical and irregular particles with deposition of trace amounts of Cu and Iodine. Alternatively, in the 50%Al-CuO–50%Al-I2O5 and 75%Al-CuO–25% Al-I2O5 formulations, smaller particle size distribution was noted (Figure 18-19), expectably due to lower amounts of I2O5 which resulted in less energetic reactions as the pressure discharge testing showed (Figure 15).

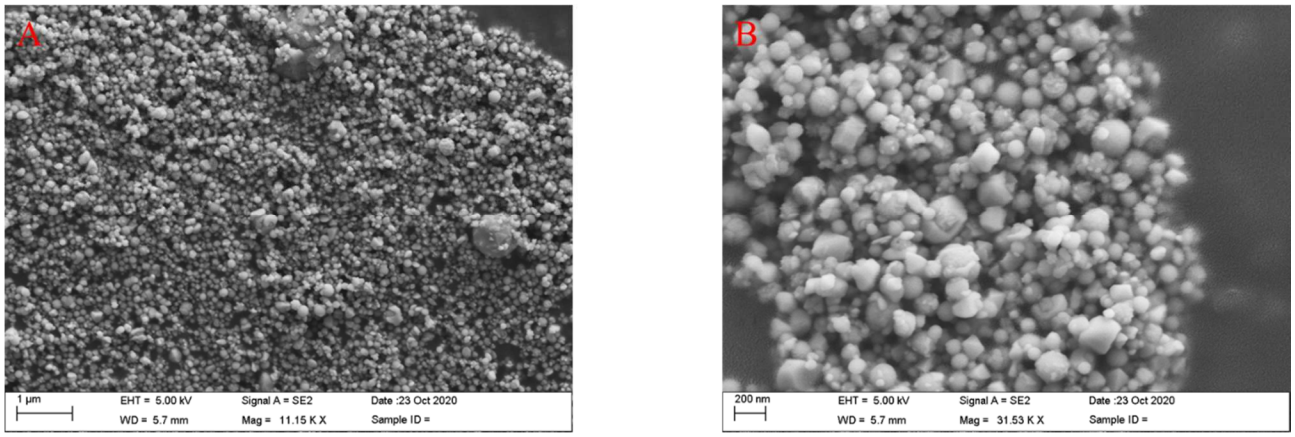

Figure 18: SEM images of the 50%Al-CuO–50%Al-I2O5 nano-formulation.

Table 4: Weight and Atomic Percent of the Al-50%CuO-50%I2O5 NM system

Element	Weight %	Atomic %	Net Int.	Error %
O	45.44	58.41	665.57	5.99
Al	54.56	41.59	532.98	6.26

Note that the size distribution is very uniform in the 50%Al-CuO–50%Al-I2O5 product sample (Figure 18) compared to the sample from the 25%Al-CuO–75%Al-I2O5 sample which was largely composed of aluminum. In addition, the 50%Al-CuO–50%Al-I2O5 sample is composed of largely spherical particles with some irregularities in morphology. Similarly, the 25%Al-CuO–75%Al-I2O5 sample had uniform particle size distribution (Figure 17).

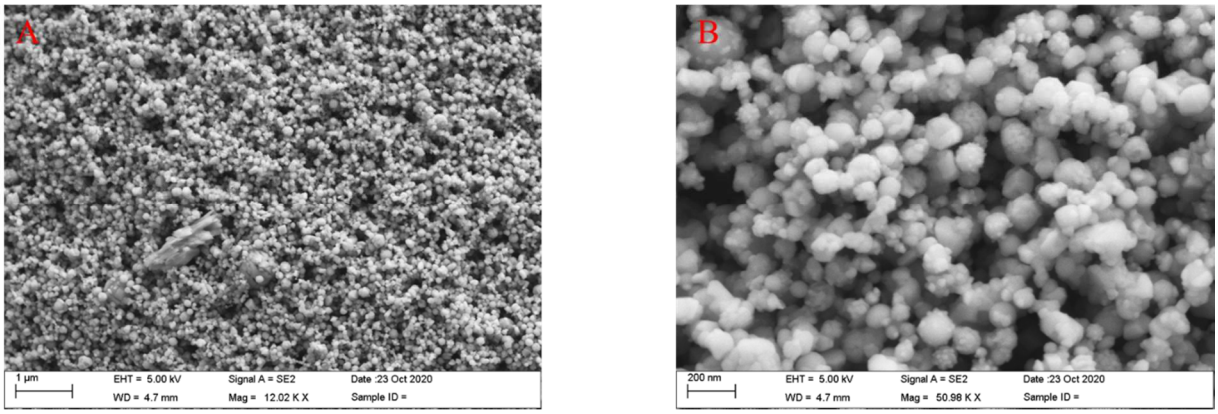

Figure 19: SEM images of the 75%Al-CuO–25%Al-I2O5 nano-formulation.

Table 5: Weight and Atomic Percent of the Al-75%CuO-25%I2O5 NM system

Element	Weight %	Atomic %	Net Int.	Error %
I	1.64	0.38	3.18	14.55
O	23.10	42.49	409.25	6.97
Cu	52.36	24.25	435.40	5.63
Al	17.09	18.64	193.55	9.15

4.5 Biocidal Test of 50%Al-CuO – 50%Al-I2O5

The reaction was carried out under a fume hood for safety and recorded using a Casio EX-ZR1200 with 960 fps recording speed to view the dispersion of the gases within the chamber (Figure 20). The video footage provided confirmation of the thermodynamic analysis, showing the rapid generation of vaporized oxidizer species. After incubation for 24 hours, the plates were

removed and observed for any E. coli growth. The number of colonies were counted to compare to a control plate which had not been exposed to the NM reaction (Figure 20).

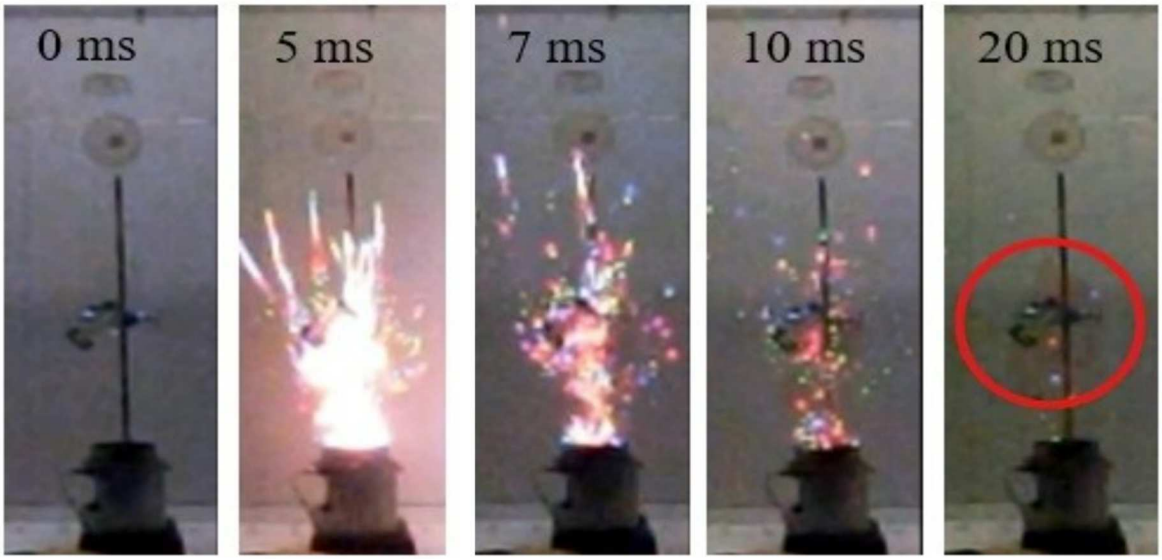

Figure 20: Frames from the slowmotion video of the NM reaction.

Table 6: Images of the agar plates exposed to the nanoenergetic reaction within the testing chamber and their respective % inhibition of E. coli colony formation.

Plate	Control	Above Reaction	Top Face	Left Face	Right Face	Front Face	Back Face
Percent Inhibition of Colony Formation	0% 	100% 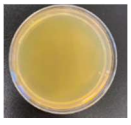	100% 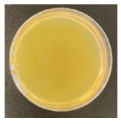	98% 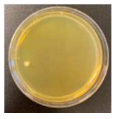	94% 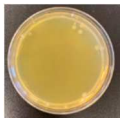	99% 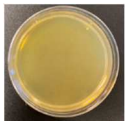	99% 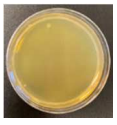

The agar plate just above the reaction as well as the plate at the top face of the chamber both experienced complete destruction of the E. coli, as even after incubation for 24 hours there

were no visible colonies that formed. While the plates fixed to the other faces of the testing chamber did not experience complete colony inhibition, the results largely support the application of the NM for biocidal applications. Since the NM charge mass was placed at the base of the chamber, the gases were rapidly expelled upwards, which is likely why the agar plates on the top face and above the reaction experienced 100% inhibition of colony formation along with them being exposed to the pressure and gases produced.

4.6 Crystallinity of SPIONs

The dextran-coated SPIONs produced by microfluidic-assisted coprecipitation exhibited characteristics peaks for Fe3O4 (Figure 21); however, there was broadening which can be explained by the use of dextran as a surfactant. Dextran, being a semi-crystalline polymer, offers the advantage of serving as a template for the growth of the SPIONs, but while it allows for more precise control of particle size, the dextran itself contributes to an increase in overall particle size; though this can be controlled by not only varying its concentration but by varying the flow rate. Note that Ohannesian et al. found that for microfluidic assisted coprecipitation, increases in pH beyond 8 mols (the required concentration for coprecipitation) were not as important as the percentage of dextran or flow rate for tuning particle size. Rather, slower flow rates and lower percentages of dextran correlated with increases in particle size while faster flow rates and decreases in the percentage of dextran correlated with decreased particle size (Ohannesian et al., 2019).

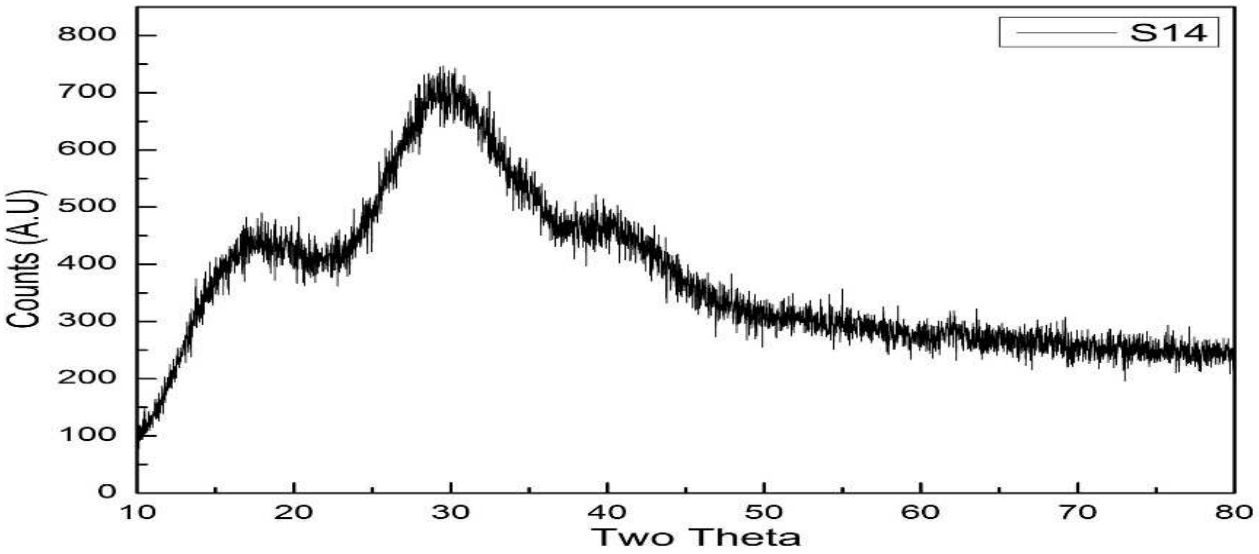

Figure 21: XRD of Dextran-Coated Iron Oxide Nanoparticles

CHAPTER V

CONCLUSION

Nanomaterials have a variety of applications in many fields, though the biomedical field particularly, has experienced an increasing amount of interest. Our work has demonstrated that a nanoenergetic material consisting of Aluminum, Copper (II) oxide, and Iodine pentoxide was effective at destroying E. coli. It has reported that E. coli can survive pressure of up to 800 MPa (Patterson, 2014), so it is unlikely that the pressure generated during the NM reaction was responsible for their destruction. Rather, the Cu and I gases that were transiently formed, followed by the CuI product depositing on the plates was responsible for producing the observed biocidal defeat. Due to the agar plates being placed at various locations within the testing chamber, near complete (98%) destruction of the bacteria highlights the excellent disinfection capabilities offered by the NM. Characterization of the product of the NM reaction displayed that CuI was produced in varying amounts depending on the initial oxidizer ratios. It has been reported that CuI has been shown to be antimicrobial, further supporting the results. In addition, microfluidics were used to produce SPIONs which have great potential for implementation in cancer treatment via magnetic hyperthermia. As a proof of concept, we have shown that SPIONs are useful for tuning the release of minocycline, an anti-cancer medication, from a PLGA scaffold within an alternating magnetic field.

Additional work characterizing the in vitro efficacy of the PLGA-minocycline-SPION drug is underway. Thus, the SPIONs produced via microfluidics have high potential for use in a variety of applications, which can be investigated in future work. Such potential applications include site-specific treatment of tumors in model animals to assess the anti-tumor efficacy of the dextran-coated SPIONs under varying strength magnetic fields, as well as how alternative surface coatings such as PEEK (Ohannesian, 2018) effect the properties. In addition, the NM offers potential future investigations; specifically, whether the biocidal effect varies from gram-negative bacteria (such as E. coli) to gram-positive bacteria. Further, plans have been made to investigate the virucidal capabilities of the NM, by modifying the testing chamber to include an inlet through which an aerosolized virus can be introduced to plated human cells (corresponding to the virus), right before detonation of the charge mass. Though it has been reported that a copper iodine complex has been used for the inactivation of SARS-CoV-2 (Mantlo et al., 2020), that was assessed in solution; thus, it would be beneficial to determine if our NM has potential as a spatial virucide by repeating the experiment with SARS-CoV-2 or a physically similar virus such as the Influenza virus.

REFERENCES

Abad, F. X.; Villena, C.; Guix, S.; Caballero, S.; Pintó, R. M.; Bosch, A. Potential Role of Fomites in the Vehicular Transmission of Human Astroviruses. *Appl. Environ. Microbiol.* 2001, *67* (9), 3904–3907.

Arriaga, M. A.; Enriquez, D. M.; Salinas, A. D.; Garcia, R., Jr; Trevino De Leo, C.; Lopez, S. A.; Martirosyan, K. S.; Chew, S. A. Application of Iron Oxide Nanoparticles to Control the Release of Minocycline for the Treatment of Glioblastoma. *Future Med. Chem.* 2021, *13* (21), 1833–1843. https://doi.org/10.4155/fmc-2021-0098.

Axel Kramer, O. A. *Use of Biocidal Surfaces for Reduction of Healthcare Acquired Infections*; Borkow, G., Ed.; Springer International Publishing: Cham, Switzerland, 2014.

Balaban, N. Q.; Merrin, J.; Chait, R.; Kowalik, L.; Leibler, S. Bacterial Persistence as a Phenotypic Switch. *Science* 2004, *305* (5690), 1622–1625.

Bera, S.; Mondal, D. *Drug Targeting and Stimuli Sensitive Drug Delivery Systems*; Grumezescu, A. M., Ed.; William Andrew Publishing: Norwich, CT, 2018.

Bertotti, G. *Hysteresis in Magnetism: For Physicists, Materials Scientists, and Engineers*; Academic Press: San Diego, CA, 1998.

BioRender http://Biorender.com (accessed 2022 -02 -22).

Blair, J.M., Webber, M.A., Baylay, A.J., Ogbolu, D.O., and Piddock, L.J. Molecular Mechanisms of Antibiotic Resistance. *Nature Review Microbio* 2015, *13*, 42–51

Blundell, S. J. Micromagnetism and the Microstructure of Ferromagnetic Solids, by Helmut Kronmüller and Manfred Fähnle: Scope: Monograph. Level: Researcher. *Contemp. Phys.* 2011, *52* (2), 157–157. https://doi.org/10.1080/00107514.2010.534181.

Bow, H.; Hwang, L. S.; Schildhaus, N.; Xing, J.; Murray, L.; Salditch, Q.; Ye, X.; Zhang, Y.; Weingart, J.; Brem, H.; Tyler, B. Local Delivery of Angiogenesis-Inhibitor Minocycline Combined with Radiotherapy and Oral Temozolomide Chemotherapy in 9L Glioma: Laboratory Investigation. *J. Neurosurg.* 2014, *120* (3), 662–669. https://doi.org/10.3171/2013.11.JNS13556.

Brown, W. F. Thermal Fluctuations of a Single-Domain Particle. *Phys. Rev.* 1963, *130* (5), 1677–1686. https://doi.org/10.1103/physrev.130.1677.

Casanova, L. M.; Jeon, S.; Rutala, W. A.; Weber, D. J.; Sobsey, M. D. Effects of Air Temperature and Relative Humidity on Coronavirus Survival on Surfaces. *Appl. Environ. Microbiol.* 2010, *76* (9), 2712–2717.

CDC. Science brief: SARS-CoV-2 and surface (fomite) transmission for indoor community environments https://www.cdc.gov/coronavirus/2019-ncov/more/science-and-research/surface-transmission.html (accessed Sep 2, 2021).

Chakraborty, S.; Rahman, T. The Difficulties in Cancer Treatment. Ecancer medical science 2012, 6, ed 16.

Chen, M.; Wei, J.; Xie, S.; Tao, X.; Zhang, Z.; Ran, P.; Li, X. Bacterial Biofilm Destruction by Size/Surface Charge-Adaptive Micelles. *Nanoscale* 2019, *11* (3), 1410–1422. https://doi.org/10.1039/c8nr05575k.

Clark, B. R.; Pantoya, M. L. The Aluminium and Iodine Pentoxide Reaction for the Destruction of Spore Forming Bacteria. *Phys. Chem. Chem. Phys.* 2010, *12* (39), 12653–12657.

Cullity, B. D. *Elements of X-Ray Diffraction*; Addison Wesley: Boston, MA, 1957.

Dikomey, E.; Becker, W.; Wielckens, K. Reduction of DNA-Polymerase Beta Activity of CHO Cells by Single and Combined Heat Treatments. *Int. J. Radiat. Biol. Relat. Stud. Phys. Chem. Med.* 1987, *52* (5), 775–785. https://doi.org/10.1080/09553008714552291.

Dlott, D. D. Thinking Big (and Small) about Energetic Materials. *Mater. Sci. Technol.* 2006, *22* (4), 463–473.

Donald G. Barceloux & Dr. Donald Barceloux. Copper. *Journal of Toxicology: Clinic* 1999, *37* (2), 217–230.

Echlin, P. *Handbook of Sample Preparation for Scanning Electron Microscopy and X-Ray Microanalysis*, 2009th ed.; Springer: New York, NY, 2011.

Eggers, M.; Eickmann, M.; Zorn, J. Rapid and Effective Virucidal Activity of Povidone-Iodine Products against Middle East Respiratory Syndrome Coronavirus (MERS-CoV) and Modified Vaccinia Virus Ankara (MVA). *Infect. Dis. Ther.* 2015, *4* (4), 491–501. https://doi.org/10.1007/s40121-015-0091-9.

Elguindi, J.; Wagner, J.; Rensing, C. Genes Involved in Copper Resistance Influence Survival of Pseudomonas Aeruginosa on Copper Surfaces. *J. Appl. Microbiol.* 2009, *106* (5), 1448–1455.

Eppink, B.; Krawczyk, P. M.; Stap, J.; Kanaar, R. Hyperthermia-Induced DNA Repair Deficiency Suggests Novel Therapeutic Anti-Cancer Strategies. *Int. J. Hyperthermia* 2012, *28* (6), 509–517. https://doi.org/10.3109/02656736.2012.695427.

Estelrich, J.; Sánchez-Martín, M. J.; Busquets, M. A. Nanoparticles in Magnetic Resonance Imaging: From Simple to Dual Contrast Agents. *Int. J. Nanomedicine* 2015, *10*, 1727–1741. https://doi.org/10.2147/IJN.S76501.

Faúndez, G.; Troncoso, M.; Navarrete, P.; Figueroa, G. Antimicrobial Activity of Copper Surfaces against Suspensions of Salmonella Enterica and Campylobacter Jejuni. *BMC Microbiol.* 2004, *4*, 19.

Festa, R. A.; Thiele, D. J. Copper: An Essential Metal in Biology. *Curr. Biol.* 2011, *21* (21), R877-83.

Forier, K.; Raemdonck, K.; De Smedt, S. C.; Demeester, J.; Coenye, T.; Braeckmans, K. Lipid and Polymer Nanoparticles for Drug Delivery to Bacterial Biofilms. *J. Control. Release* 2014, *190*, 607–623. https://doi.org/10.1016/j.jconrel.2014.03.055.

Frazier, J. L.; Wang, P. P.; Case, D.; Tyler, B. M.; Pradilla, G.; Weingart, J. D.; Brem, H. Local Delivery of Minocycline and Systemic BCNU Have Synergistic Activity in the Treatment of Intracranial Glioma. *J. Neurooncol.* 2003, *64* (3), 203–209. https://doi.org/10.1023/a:1025695423097.

Fung, M. C.; Bowen, D. L. Silver Products for Medical Indications: Risk-Benefit Assessment. *J. Toxicol. Clin. Toxicol.* 1996, *34* (1), 119–126.

Goya, G. F.; Lima, E., Jr; Arelaro, A. D.; Torres, T. E.; Rechenberg, H. R.; Rossi, L.; Marquina, C.; Ibarra, M. R. Magnetic Hyperthermia with Fe3O4 Nanoparticles: The Influence of Particle Size on Energy Absorption. *arXiv [cond-mat.mtrl-sci]*, 2013.

Grass, G.; Rensing, C.; Solioz, M. Metallic Copper as an Antimicrobial Surface. *Appl. Environ. Microbiol.* 2011, *77* (5), 1541–1547.]

Hajalilou, A.; Ferreira, L. P.; Melo Jorge, M. E.; Reis, C. P.; Cruz, M. M. Superparamagnetic Ag-Fe3O4 Composites Nanoparticles for Magnetic Fluid Hyperthermia. *J. Magn. Magn. Mater.* 2021, *537* (168242), 168242.

Hall, E. J.; Roizin-Towle, L. Biological Effects of Heat https://cancerres.aacrjournals.org/content/44/10_Supplement/4708s.full-text.pdf (accessed Jan 17, 2022).

Harrison, P. H.; Hoare, R. *Metals in Biochemistry*; Chapman and Hall: London, England, 1980.

Hergt, R.; Dutz, S. Magnetic Particle Hyperthermia—Biophysical Limitations of a Visionary Tumour Therapy. *J. Magn. Magn. Mater.* 2007, *311* (1), 187–192

Hobosyan, M. A.; Martirosyan, K. S. Iodine Pentoxide Nano-Rods for High Density Energetic Materials. *Propellants Explos. Pyrotech.* 2017, *42* (5), 506–513.

Hobosyan, M. A.; Martirosyan, K. S. Novel Nanoenergetic Materials: Emerging Trends and Applications. *IEEE Nanotechnol. Mag.* 2020, *14* (1), 30–36.

Hobosyan, M. A.; Yolchinyan, S. A.; Martirosyan, K. S. A Novel Nano-Energetic System Based on Bismuth Hydroxide. *RSC Adv.* 2016, *6* (71), 66564–66570.

Hyperthermia to treat cancer https://www.cancer.gov/about-cancer/treatment/types/hyperthermia (accessed Jan 10, 2022).

Iliakis, G.; Wu, W.; Wang, M. DNA Double Strand Break Repair Inhibition as a Cause of Heat Radiosensitization: Re-Evaluation Considering Backup Pathways of NHEJ. *Int. J. Hyperthermia* 2008, *24* (1), 17–29. https://doi.org/10.1080/02656730701784782.

Inesi, G. Molecular Features of Copper Binding Proteins Involved in Copper Homeostasis. *IUBMB Life* 2017, *69* (4), 211–217.

Jha, S.; Sharma, P. K.; Malviya, R. Hyperthermia: Role and Risk Factor for Cancer Treatment. *Achiev. Life Sci.* 2016, *10* (2), 161–167. https://doi.org/10.1016/j.als.2016.11.004.

Jung, S.-H.; Ryu, C.-M.; Kim, J.-S. Bacterial Persistence: Fundamentals and Clinical Importance. *J. Microbiol.* 2019, *57* (10), 829–835.

Kantidze, O. L.; Velichko, A. K.; Luzhin, A. V.; Razin, S. V. Heat Stress-Induced DNA Damage. *Acta Naturae* 2016, *8* (2), 75–78.

Karen S. Martirosyan, Mkhitar Hobosyan, Alexander Kazansky. *Nanostructured Thermites Based on Iodine Pentoxide for Bio Agent Defeat Systems*; 2011.

Karlin, K. D. Metalloenzymes, Structural Motifs, and Inorganic Models. *Science* 1993, *261* (5122), 701–708.

Karthickraja, D.; Karthi, S.; Kumar, G. A.; Sardar, D. K.; Dannangoda, G. C.; Martirosyan, K. S.; Girija, E. K. Fabrication of Core–Shell CoFe2O4@HAp Nanoparticles: A Novel Magnetic Platform for Biomedical Applications. *New J Chem* 2019, *43* (34), 13584–13593. https://doi.org/10.1039/c9nj02510c.

Kim, J.-S.; Yamasaki, R.; Song, S.; Zhang, W.; Wood, T. K. Single Cell Observations Show Persister Cells Wake Based on Ribosome Content: Ribosome Content Dictates Persister Cell Waking. *Environ. Microbiol.* 2018, *20* (6), 2085–2098.

Kou, J. H.; Emmett, C.; Shen, P.; Aswani, S.; Iwamoto, T.; Vaghefi, F.; Cain, G.; Sanders, L. Bioerosion and Biocompatibility of Poly(d,l-Lactic-Co-Glycolic Acid) Implants in Brain. *J. Control. Release* 1997, *43* (2–3), 123–130. https://doi.org/10.1016/s0168-3659(96)01477-0.

Landis, R. F.; Gupta, A.; Lee, Y.-W.; Wang, L.-S.; Golba, B.; Couillaud, B.; Ridolfo, R.; Das, R.; Rotello, V. M. Cross-Linked Polymer-Stabilized Nanocomposites for the Treatment of Bacterial Biofilms. *ACS Nano* 2017, *11* (1), 946–952. https://doi.org/10.1021/acsnano.6b07537.

Laurent, S.; Dutz, S.; Häfeli, U. O.; Mahmoudi, M. Magnetic Fluid Hyperthermia: Focus on Superparamagnetic Iron Oxide Nanoparticles. *Adv. Colloid Interface Sci.* 2011, *166* (1–2), 8–23.

Lei, H., Jones, R. M., & Li, Y. (2017). Exploring surface cleaning strategies in hospital to prevent contact transmission of methicillin-resistant Staphylococcus aureus. *BMC Infectious Diseases*, *17*(1), 85.

Lemire, J. A.; Harrison, J. J.; Turner, R. J. Antimicrobial Activity of Metals: Mechanisms, Molecular Targets and Applications. *Nat. Rev. Microbiol.* 2013, *11* (6), 371–384.

Makabenta, J. M. V.; Nabawy, A.; Li, C.-H.; Schmidt-Malan, S.; Patel, R.; Rotello, V. M. Nanomaterial-Based Therapeutics for Antibiotic-Resistant Bacterial Infections. *Nat. Rev. Microbiol.* 2021, *19* (1), 23–36. https://doi.org/10.1038/s41579-020-0420-1.

Malek, I.; Schaber, C. F.; Heinlein, T.; Schneider, J. J.; Gorb, S. N.; Schmitz, R. A. Vertically Aligned Multi Walled Carbon Nanotubes Prevent Biofilm Formation of Medically

Relevant Bacteria. *J. Mater. Chem. B Mater. Biol. Med.* 2016, *4* (31), 5228–5235. https://doi.org/10.1039/c6tb00942e.

Mantlo, E.; Rhodes, T.; Boutros, J.; Patterson-Fortin, L.; Evans, A.; Paessler, S. In Vitro Efficacy of a Copper Iodine Complex PPE Disinfectant for SARS-CoV-2 Inactivation. *F1000Res.* 2020, *9*, 674.

Martinez-Boubeta, C.; Simeonidis, K.; Makridis, A.; Angelakeris, M.; Iglesias, O.; Guardia, P.; Cabot, A.; Yedra, L.; Estradé, S.; Peiró, F.; Saghi, Z.; Midgley, P. A.; Conde-Leborán, I.; Serantes, D.; Baldomir, D. Learning from Nature to Improve the Heat Generation of Iron-Oxide Nanoparticles for Magnetic Hyperthermia Applications. *Sci. Rep.* 2013, *3* (1), 1652. https://doi.org/10.1038/srep01652.

Marx, D. E.; Barillo, D. J. Silver in Medicine: The Basic Science. *Burns* 2014, *40 Suppl 1*, S9–S18.

Massey, R. C.; Buckling, A.; Peacock, S. J. Phenotypic Switching of Antibiotic Resistance Circumvents Permanent Costs in Staphylococcus Aureus. *Curr. Biol.* 2001, *11* (22), 1810–1814.

Matea, C. T.; Mocan, T.; Tabaran, F.; Pop, T.; Mosteanu, O.; Puia, C.; Iancu, C.; Mocan, L. Quantum Dots in Imaging, Drug Delivery and Sensor Applications. *Int. J. Nanomedicine* 2017, *12*, 5421–5431. https://doi.org/10.2147/IJN.S138624.

Mehtar, S.; Wiid, I.; Todorov, S. D. The Antimicrobial Activity of Copper and Copper Alloys against Nosocomial Pathogens and Mycobacterium Tuberculosis Isolated from Healthcare Facilities in the Western Cape: An in-Vitro Study. *J. Hosp. Infect.* 2008, *68* (1), 45–51.

Mei, L.; Lu, Z.; Zhang, X.; Li, C.; Jia, Y. Polymer-Ag Nanocomposites with Enhanced Antimicrobial Activity against Bacterial Infection. *ACS Appl. Mater. Interfaces* 2014, *6* (18), 15813–15821. https://doi.org/10.1021/am502886m.

Michels, H. T.; Noyce, J. O.; Keevil, C. W. Effects of Temperature and Humidity on the Efficacy of Methicillin-Resistant Staphylococcus Aureus Challenged Antimicrobial Materials Containing Silver and Copper. *Lett. Appl. Microbiol.* 2009, *49* (2), 191–195.

Mitchell, E. Pathogen, persistence, and prevalence http://blog.eoscu.com/blog/pathogen-persistence-and-prevalence (accessed Sep 1, 2021).

Molteni, C.; Abicht, H. K.; Solioz, M. Killing of Bacteria by Copper Surfaces Involves Dissolved Copper. *Appl. Environ. Microbiol.* 2010, *76* (12), 4099–4101.

Mondal, S.; Manivasagan, P.; Bharathiraja, S.; Santha Moorthy, M.; Kim, H. H.; Seo, H.; Lee, K. D.; Oh, J. Magnetic Hydroxyapatite: A Promising Multifunctional Platform for Nanomedicine Application. *Int. J. Nanomedicine* 2017, *12*, 8389–8410. https://doi.org/10.2147/IJN.S147355.

Moroz, P.; Jones, S. K.; Gray, B. N. Magnetically Mediated Hyperthermia: Current Status and Future Directions. *Int. J. Hyperthermia* 2002, *18* (4), 267–284. https://doi.org/10.1080/02656730110108785.

Murray, P. R.; Rosenthal, K. S.; Pfaller, M. A. *Medical Microbiology*, 8th ed.; Elsevier, 2015.

Murthy, S. K. Nanoparticles in Modern Medicine: State of the Art and Future Challenges. *Int. J. Nanomedicine* 2007, *2* (2), 129–141.

Nanomagnetism: Applications and Perspectives, 1st ed.; Fermon, C., Van de Voorde, M., Eds.; Van de Voorde, M., Series Ed.; Wiley-VCH Verlag: Weinheim, Germany, 2017.

Néel, L. Théorie Du Traînage Magnétique de Diffusion. *[Journal phys. Radium]* 1952, *13* (5), 249–264. https://doi.org/10.1051/jphysrad:01952001305024900.

Nemati, Z.; Das, R.; Alonso, J.; Clements, E.; Phan, M. H.; Srikanth, H. Iron Oxide Nanospheres and Nanocubes for Magnetic Hyperthermia Therapy: A Comparative Study. *J. Electron. Mater.* 2017, *46* (6), 3764–3769. https://doi.org/10.1007/s11664-017-5347-6.

NIH National Cancer Institute. Cancer Statistics https://www.cancer.gov/about-cancer/understanding/statistics (accessed Dec 8, 2021).

Nikitin, A.; Khramtsov, M.; Garanina, A.; Mogilnikov, P.; Sviridenkova, N.; Shchetinin, I.; Savchenko, A.; Abakumov, M.; Majouga, A. Synthesis of Iron Oxide Nanorods for Enhanced Magnetic Hyperthermia. *J. Magn. Magn. Mater.* 2019, *469*, 443–449. https://doi.org/10.1016/j.jmmm.2018.09.014.

Nogrady, T.; Weaver, D. F. *Medicinal Chemistry: A Molecular and Biochemical Approach*, 3rd ed.; Oxford University Press: New York, NY, 2005.

Noyce, J. O.; Michels, H.; Keevil, C. W. Inactivation of Influenza A Virus on Copper versus Stainless Steel Surfaces. *Appl. Environ. Microbiol.* 2007, *73* (8), 2748–2750.

Noyce, J. O.; Michels, H.; Keevil, C. W. Potential Use of Copper Surfaces to Reduce Survival of Epidemic Meticillin-Resistant Staphylococcus Aureus in the Healthcare Environment. *J. Hosp. Infect.* 2006, *63* (3), 289–297.

Noyce, J. O.; Michels, H.; Keevil, C. W. Use of Copper Cast Alloys to Control Escherichia Coli O157 Cross-Contamination during Food Processing. *Appl. Environ. Microbiol.* 2006, *72* (6), 4239–4244.

Ohannesian, N. MAGNETIC POLYMER COMPOSITE AS A THERMOSENSITIVE AGENT FOR INDUCED HYPERTHERMIA, University of Texas Rio Grande Valley, Brownsville, Texas, 2018.

Ohannesian, N.; De Leo, C. T.; Martirosyan, K. S. Dextran Coated Superparamagnetic Iron Oxide Nanoparticles Produced by Microfluidic Process. *Mater. Today* 2019, *13*, 397–403. https://doi.org/10.1016/j.matpr.2019.03.172.

Osme, S. F.; de Souza, J. M.; Osme, I. T.; Almeida, A. P. S.; Arantes, A.; Mendes-Rodrigues, C.; Gontijo Filho, P. P.; Ribas, R. M. Financial Impact of Healthcare-Associated Infections (HAI) on Intensive Care Units (ICUs) Estimated for Fifty Brazilian University Hospitals, Affiliated to the Unified Health System (SUS). *J. Hosp. Infect.* 2021. https://doi.org/10.1016/j.jhin.2021.08.012.

Patterson, M. High-Pressure Treatment of Foods. In *Encyclopedia of Food Microbiology*; Elsevier, 2014; pp 206–212.

Polini, A.; Yang, F. Physicochemical Characterization of Nanofiber Composites. In *Nanofiber Composites for Biomedical Applications*; Ramalingam, M., Ramakrishna, S., Eds.; Elsevier, 2017; pp 97–115.

Pucci, C.; Martinelli, C.; Ciofani, G. Innovative Approaches for Cancer Treatment: Current Perspectives and New Challenges. *Ecancermedicalscience* 2019, *13*, 961. https://doi.org/10.3332/ecancer.2019.961.

Puszynski, J. A.; Bulian, C. J.; Swiatkiewicz, J. J. Processing and Ignition Characteristics of Aluminum-Bismuth Trioxide Nanothermite System. *J. Propuls. Power* 2007, *23* (4), 698–706.

Quaranta, D.; Krans, T.; Espírito Santo, C.; Elowsky, C. G.; Domaille, D. W.; Chang, C. J.; Grass, G. Mechanisms of Contact-Mediated Killing of Yeast Cells on Dry Metallic Copper Surfaces. *Appl. Environ. Microbiol.* 2011, *77* (2), 416–426.

Rezanezhad, A.; Hajalilou, A.; Eslami, F.; Parvini, E.; Abouzari-Lotf, E.; Aslibeiki, B. Superparamagnetic Magnetite Nanoparticles for Cancer Cells Treatment via Magnetic Hyperthermia: Effect of Natural Capping Agent, Particle Size and Concentration. *J. Mater. Sci.: Mater. Electron.* 2021, *32* (19), 24026–24040.

Ron, E. Z. Bacterial Stress Response. In *The Prokaryotes*; Springer New York: New York, NY, 2006; pp 1012–1027.

S. Martirosyan, K. Thermosensitive Magnetic Nanoparticles for Self-Controlled Hyperthermia Cancer Treatment. *J. Nanomed. Nanotechnol.* 2012, *03* (06). https://doi.org/10.4172/2157-7439.1000e112.

Santo, C. E.; Morais, P. V.; Grass, G. Isolation and Characterization of Bacteria Resistant to Metallic Copper Surfaces. *Appl. Environ. Microbiol.* 2010, *76* (5), 1341–1348.

Shiryaev, A. A. Distinctive Features of Thermodynamic Analysis in SHS Investigations. *J. eng. phys. thermophys.* 1993, *65* (4), 957–962.

Shiryaev, A. A. Thermodynamics of SHS Processes: Advanced Approach. *Int. J. Self-Propag. High-Temp. Synth* 1995, *4, 4*, 351–362.

Silvestry-Rodriguez, N.; Sicairos-Ruelas, E. E.; Gerba, C. P.; Bright, K. R. Silver as a Disinfectant. In *Reviews of Environmental Contamination and Toxicology*; Springer New York: New York, NY, 2007; pp 23–45.

Soetaert, F.; Korangath, P.; Serantes, D.; Fiering, S.; Ivkov, R. Cancer Therapy with Iron Oxide Nanoparticles: Agents of Thermal and Immune Therapies. *Adv. Drug Deliv. Rev.* 2020, *163–164*, 65–83.

Sun, J.; Pantoya, M. L.; Simon, S. L. Dependence of Size and Size Distribution on Reactivity of Aluminum Nanoparticles in Reactions with Oxygen and MoO3. *Thermochim. Acta* 2006, *444* (2), 117–127

Tamayo, L.; Azócar, M.; Kogan, M.; Riveros, A.; Páez, M. Copper-Polymer Nanocomposites: An Excellent and Cost-Effective Biocide for Use on Antibacterial Surfaces. *Mater. Sci. Eng. C Mater. Biol. Appl.* 2016, *69*, 1391–1409.

Theraud, M., Gangneux, J.P., Preney, L., Guigen, C. Comparative Survival of Clinical and Environmental Isolates of Candida Albicans and Cryptococcus Neoformans in Natural and Experimental Conditions. *journal medical mycology* 2003, *13* (2), 93–97.

V.D., Bergh, B., Fauvart, M., and Michiels, J. Formation, Physiology, Ecology, Evolution and Clinical Importance of Bacterial Persisters. *FEMS Mic* 2017, *41*, 219–251

Valko, M.; Morris, H.; Cronin, M. T. D. Metals, Toxicity and Oxidative Stress. *Curr. Med. Chem.* 2005, *12* (10), 1161–1208.

van Rhoon, G. C.; Samaras, T.; Yarmolenko, P. S.; Dewhirst, M. W.; Neufeld, E.; Kuster, N. CEM43°C Thermal Dose Thresholds: A Potential Guide for Magnetic Resonance Radiofrequency Exposure Levels? *Eur. Radiol.* 2013, *23* (8), 2215–2227. https://doi.org/10.1007/s00330-013-2825-y.

Wada, H.; Nojima, Y.; Ogawa, S.; Hayashi, N.; Sugiyama, N.; Kajiura, T.; Ueda, T.; Morimoto, S.; Yokota, K. Relationship between Virucidal Efficacy and Free Iodine Concentration of Povidone-Iodine in Buffer Solution. *Biocontrol Sci.* 2016, *21* (1), 21–27. https://doi.org/10.4265/bio.21.21

Wadhera, A.; Fung, M. Systemic Argyria Associated with Ingestion of Colloidal Silver. *Dermatol. Online J.* 2005, *11* (1), 12.

Warnes, S. L.; Green, S. M.; Michels, H. T.; Keevil, C. W. Biocidal Efficacy of Copper Alloys against Pathogenic Enterococci Involves Degradation of Genomic and Plasmid DNAs. *Appl. Environ. Microbiol.* 2010, *76* (16), 5390–5401.

Weaver, L.; Michels, H. T.; Keevil, C. W. Potential for Preventing Spread of Fungi in Air-Conditioning Systems Constructed Using Copper Instead of Aluminium: Copper in HVAC Systems to Control Fungi. *Lett. Appl. Microbiol.* 2010, *50* (1), 18–23.

Weaver, L.; Michels, H. T.; Keevil, C. W. Survival of Clostridium Difficile on Copper and Steel: Futuristic Options for Hospital Hygiene. *J. Hosp. Infect.* 2008, *68* (2), 145–151.

Weber, D. J.; Rutala, W. A. Self-Disinfecting Surfaces: Review of Current Methodologies and Future Prospects. *Am. J. Infect. Control* 2013, *41* (5 Suppl), S31-5.

Weingart, J. D.; Sipos, E. P.; Brem, H. The Role of Minocycline in the Treatment of Intracranial 9L Glioma. *J. Neurosurg.* 1995, *82* (4), 635–640. https://doi.org/10.3171/jns.1995.82.4.0635

Wheeldon, L. J.; Worthington, T.; Lambert, P. A.; Hilton, A. C.; Lowden, C. J.; Elliott, T. S. J. Antimicrobial Efficacy of Copper Surfaces against Spores and Vegetative Cells of Clostridium Difficile: The Germination Theory. *J. Antimicrob. Chemother.* 2008, *62* (3), 522–525.

Wilks, S. A.; Michels, H. T.; Keevil, C. W. Survival of Listeria Monocytogenes Scott A on Metal Surfaces: Implications for Cross-Contamination. *Int. J. Food Microbiol.* 2006, *111* (2), 93–98.

Wilks, S. A.; Michels, H.; Keevil, C. W. The Survival of Escherichia Coli O157 on a Range of Metal Surfaces. *Int. J. Food Microbiol.* 2005, *105* (3), 445–454.

World Health Organization (WHO). *Antimicrobial Resistance Global Report on Surveillance*; World Health Organization: Genève, Switzerland, 2014.

Zhou, W.; Apkarian, R.; Wang, Z. L.; Joy, D. Fundamentals of Scanning Electron Microscopy (SEM). In *Scanning Microscopy for Nanotechnology*; Springer New York: New York, NY, 2006; pp 1–40.

BIOGRAPHICAL SKETCH

Silverio Lopez is currently enrolled in the Physician's Assistant Program at the University of Texas Rio Grande Valley. He has completed a Master of Science in Biochemistry and Molecular Biology with the University of Texas at Rio Grande Valley. He began his graduate studies in the Fall of 2020 and completed the degree by Spring of 2022. Silverio Lopez worked under Dr. Karen Martirosyan in nanoscience research, working to understand the relatedness between multiple scientific disciplines. Graduate research in the nanoscience laboaratory led to the development of his skills in material characterization. He has shown interest working on projects that explore the biomedical applications of magnetic and hybrid nanoparticles. Permanent email address Silverio.lopez98@yahoo.com